Quasicontinuum-based multiscale approaches for plate-like beam lattices experiencing in-plane and out-of-plane deformation

L.A.A. Beex[a,*], P. Kerfriden[a], T. Rabczuk[b], S.P.A. Bordas[a,c]

[a] *Cardiff University, School of Engineering, Queen's Buildings, The Parade*
Cardiff CF24 3AA, Wales, UK
[b] *Institute of Structural Mechanics, Bauhaus-University, Weimar Marienstrasse 15 99423*
Weimar, Germany
[c] *Research Unit in Engineering Science, Luxembourg University, 6 rue Richard*
Coudenhove-Kalergi, L-1359 Luxembourg

Abstract

The quasicontinuum (QC) method is a multiscale approach that aims to reduce the computational cost of discrete lattice computations. The method incorporates smallscale local lattice phenomena (e.g. a single lattice defect) in macroscale simulations. Since the method works directly and only on the beam lattice, QC frameworks do not require the construction and calibration of an accompanying continuum model (e.g. a cosserat/micropolar description). Furthermore, no coupling procedures are required between the regions of interest in which the beam lattice is fully resolved and coarse domains in which the lattice is effectively homogenized. Hence, the method is relatively straightforward to implement and calibrate. In this contribution, four variants of the QC method are investigated for their use for planar beam lattices which can also experience out-of-plane deformation. The different frameworks are compared to the direct lattice computations for three truly multiscale test cases in which a single lattice defect is present in an otherwise perfectly regular beam lattice.

Key words: quasicontinuum method, multiscale, beam, beam lattice, beam model, lattice model, network model, discrete model, cosserat, micropolar, mixed formulation

---

[*] Corresponding author
Email: L.A.A.Beex@gmail.com

Preprint submitted to Comput. methods Appl. Mech. Engrg *June 12, 2014*

1. Introduction

Lattice models using discrete springs and beams (see ahead to Fig. 1) are often used to numerically predict the mechanical behavior of materials with a discrete microstructure (Ostoja-Starzewski, 2002; Fleck and Qiu, 2007; Ryvkin and Slepyan, 2010). They are often used to investigate the mechanics of atomistic crystals (Tadmor et al., 1996a,b; Miller et al., 1998; Shimokawa et al., 2004), fibrous materials, such as textiles (Ben Boubaker et al., 2007; Lomov et al., 2007; Beex et al., 2013a), paper (Heyden, 2000; Bronkhorst, 2003; Kulachenko and Uesaka, 2012; Persson and Isaksson, 2013; Wilbrink et al., 2013), collagen networks (Chandran and Barocas, 2006; Stylianopoulos and Barocas, 2007; Argento et al., 2012) and glass-fiber networks (Ridruejo et al., 2010, 2012), and heterogeneous materials, such as concrete (Ince et al., 2002; Karihaloo et al., 2003; Lilliu and Van Mier, 2007). Their extensive use might be explained by their simplicity and discrete nature. This discreteness makes them appropriate to represent discrete meso-, micro- and nano-scale structures. Consequently, lattice models are able to capture mechanical events related to the discreteness of the structures they represent. One can think here of the nucleation of a single dislocation in metals (Tadmor et al., 1996a,b; Shenoy et al., 1999; Eidel and Stukowski, 2009), the failure of an individual fiber-to-fiber bond in collagen networks (Intrigila et al., 2007) or in paper materials (Kulachenko and Uesaka, 2012; Wilbrink et al., 2013) and the failure of a conductive wire in an electronic textile (Beex et al., 2013a).

For computations at application scales, the use of lattice models defined at small scales (e.g. the meso-scale or micro-scale) is computationally costly, if not computationally prohibitive. Multiscale approaches can be employed to increase the computational efficiency of large-scale lattice computations (e.g. Gonella and Ruzzene (2008); Zhang et al. (2010); Kerfriden et al. (2011, 2012, 2013a,b)). One of those multiscale approaches is the quasicontinuum (QC) method (Tadmor et al., 1996a,b), which has the following advantages that are not all shared by other multiscale approaches.

- The QC method allows the lattice model to be fully resolved in regions of interest so that discrete events (e.g. dislocation nucleation, fiber failure) can be captured.
- QC approaches use the lattice model in fully resolved domains as well as in coarse domains. Hence, the user does not have to formulate and cal-

ibrate an accompanying continuum description. This is in contrast to numerous other multiscale approaches in which continuum descriptions are used in coarse domains of less interest and the lattice model only in regions of interest (Curtin and Miller, 2003; Xiao and Belytschko, 2004; Klein and Zimmerman, 2006; Fish et al., 2007).

- In a number of QC approaches (as those proposed in this paper), no coupling procedures between coarse domains and fully resolved domains are required because the lattice model is used in both domains in a fully nonlocal fashion. This is in contrast to numerous other multiscale approaches that use handshaking procedures or Arlequin type of coupling procedures between continuum descriptions in coarse domains and the full lattice model in regions of interest (Curtin and Miller, 2003; Xiao and Belytschko, 2004; Klein and Zimmerman, 2006; Fish et al., 2007). Consequently, the implementation is straightforward.

A disadvantage of the method is that it can currently not be used for irregular networks, but only for regular discrete models (i.e. lattice models). Since a significant number of materials contains a regular discreteness at small length scales however, the QC method is frequently used. Even for materials that are characterized by irregular discreteness, a regular lattice, and thus the QC method, at least incorporates a degree of discreteness that cannot necessarily be guaranteed by the use of continuum models.

QC approaches have mostly been used to study the behavior of (conservative) atomistic crystals. Studies can be found that focus on fracture along grain boundaries, nanoindentation and phase transformations (Tadmor et al., 1996a,b; Miller et al., 1998; Shenoy et al., 1999; Miller and Tadmor, 2002; Shimokawa et al., 2004; Eidel and Stukowski, 2009; Dobson et al., 2012; Yang et al., 2013). Recently, QC variants were proposed that can be applied to (non-conservative) dissipative structural lattice models using springs (Beex et al., 2011, 2013b, 2014a). These variants depart from the virtual-power statement of the lattice and are therefore referred to as virtual-power-based QC approaches. Their applicability was demonstrated for structural lattice models with dissipative mechanisms in the lattice interactions (Beex et al., 2014a) and for lattice models with dissipative mechanisms in the lattice nodes (Beex et al., 2014b).

The previous QC approaches for structural lattice models (Beex et al., 2011, 2014a,b) can only treat trusses (i.e. springs). Beams however, which also have a resistance to bending in contrast to springs, are used in a large amount of structural lattice models. A few examples are beam models for graphene sheets (Berinskii and Borodich, 2013; Wang et al., 2013), paper (Heyden, 2000; Bronkhorst, 2003; Kulachenko and Uesaka, 2012; Persson and Isaksson, 2013) and concrete (Ince et al., 2002; Karihaloo et al., 2003; Lilliu and Van Mier, 2007).

Since the kinematic variables of beam lattices contain not only nodal displacement but also nodal rotations, they cannot straightforwardly be incorporated in existing QC frameworks for structural lattice models that use springs. The aim of this paper is therefore to propose a number of multiscale QC approaches for beam lattices that incorporate local discrete mechanical phenomena in regions of interest, whereas in coarse domains a significant computational gain is made. The proposed QC frameworks incorporate the nodal displacements as well as the nodal rotations.

This paper contains the following sections. In the next section the governing equations of linear elastic beam lattices are described. Afterwards, the two principles of the QC method, i.e. interpolation and summation, are addressed and how they can be used for beam lattices. The proposed QC variants for beam lattices are explained in detail as well. In section 4 the QC variants are applied to a planar beam lattice with an individual lattice defect that is separately subjected to in-plane uniform deformation, in-plane bending and out-of-plane bending. The computational gain of each framework is presented as well as the accuracy that can be achieved. Finally, conclusions are presented.

2. Large-scale beam lattices

In this section the governing equations of beam lattices and the high computational costs of large-scale beam lattices are briefly described. The derivation is limited to lattices using elastic Euler-Bernoulli beams (Han et al., 1999). In order to streamline this paper, the derivation of the potential energy (i.e. stored energy) of an individual beam in the lattice can be found in Appendix A.

Let us start with the planar beam lattice presented in Fig. 1 which is part of a large-scale beam lattice. The entire beam lattice contains b beams (stored in index set $B = \{1, ..., b\}$) and n lattice (beam) nodes (stored in index set $N = \{1, ..., n\}$). Since beams have a resistance to bending (see Appendix A), the kinematic variables associated with the lattice nodes consist of nodal displacements as well as nodal rotations. This is in contrast to the kinematic variables of lattice models consisting of springs that only contain nodal displacements.

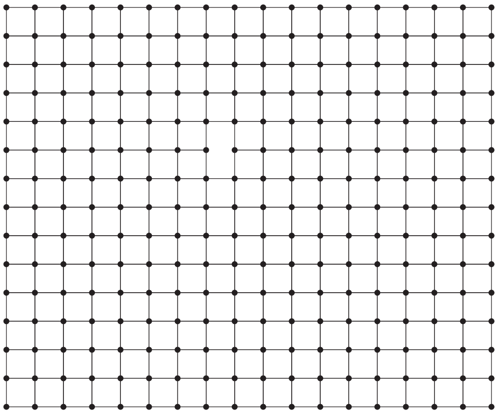

Figure 1: Part of a beam lattice consisting of square unit cells including a lattice defect.

In this study a beam can deform in three dimensions. The kinematic variables associated with lattice node i are therefore three displacements (U_i, V_i, W_i) and three rotations ($\Theta_i, \Phi_i, \Omega_i$, see Appendix A). This means that $6n$ kinematic variables are associated with the entire lattice. All $3n$ displacements are stored in column matrix $\mathbf{U}$ and the $3n$ rotations are stored in column matrix $\mathbf{\Theta}$. The displacements and rotations are stored together in one column matrix $\mathbf{a}$: $\mathbf{a} = [\mathbf{U}^T \, \mathbf{\Theta}^T]^T$ for ease of notation.

Since the beams are considered to be linear elastic in the present study, a solution for the lattice can be found by minimizing the total potential energy, E_{tot}, with respect to the degrees of freedom, i.e. the $6n$ kinematic variables:

$$\mathbf{a} = \underset{\mathbf{a}^*}{\operatorname{argmin}} \, E_{tot}(\mathbf{a}^*). \tag{1}$$

The total potential energy E_{tot} consists of an internal part, E_{int}, and an external part:

$$E_{tot}(\mathbf{a}) = E_{int}(\mathbf{a}) - \mathbf{f}_{ext}^T \mathbf{a}, \tag{2}$$

where $\mathbf{f}_{ext}$ is a column matrix of size $6n \times 1$ containing forces and moments externally applied at the lattice nodes. The external forces and moments are stored in $\mathbf{f}_{ext}$ such that they are conjugate to the degrees of freedom in $\mathbf{a}$ on which they work. The internal potential energy can be computed by summing the internal potential energy of each beam, E_i:

$$E_{int}(\mathbf{a}) = \sum_{i=1}^{b} E_i(\mathbf{a}). \tag{3}$$

Of course, the internal energy of beam i, E_i, only depends on the displacements and rotations of the two lattice nodes connected to beam i, but E_i can thus also be expressed in terms of $\mathbf{a}$. The expression for the internal energy of beam i can be found in Appendix A.

Now an expression for the total potential energy is established, we can return to the minimization thereof (Eq. (1)). The minimum principle can be written in the variational form as follows:

$$\delta E_{tot}(\mathbf{a}) = \delta \mathbf{a}^T (\mathbf{f}(\mathbf{a}) - \mathbf{f}_{ext}) = 0 \qquad \forall \delta \mathbf{a}, \tag{4}$$

where δ refers to a virtual change and $\mathbf{f}$ is a column matrix of length $6n$ that contains the derivatives of the total internal energy to the degrees of freedom (i.e. the kinematic variables). Hence, effectively $\mathbf{f}$ contains forces and moments. To establish column matrix $\mathbf{f}$, each beam in the lattice must be visited (recall Eq. (3)):

$$\mathbf{f}(\mathbf{a}) = \frac{\partial E_{int}(\mathbf{a})}{\partial \mathbf{a}} = \sum_{i=1}^{b} \frac{\partial E_i(\mathbf{a})}{\partial \mathbf{a}} = \sum_{i=1}^{b} \mathbf{f}_i(\mathbf{a}), \tag{5}$$

where the components of $\mathbf{f}_i$ are given by:

$$(f_i)_p = \frac{\partial E_i}{\partial a_p}, \tag{6}$$

and p runs over all components of $\mathbf{a}$, i.e. the degrees of freedom or kinematic variables.

Although in this study a linear elastic (convex) case is considered, we still employ a Newton-Raphson procedure to solve Eq. (4), since non-linearities can present in planar beam lattices, e.g. by using elastoplastic beams instead of linear elastic beams. Employing a Newton-Raphson procedure leads to the following formulation:

$$\delta \mathbf{a}^T(\mathbf{f}(\mathbf{a}^*) + \mathbf{K} d\mathbf{a}) = \delta \mathbf{a}^T \mathbf{f}_{ext} \qquad \forall \delta \mathbf{a}, \tag{7}$$

where $\mathbf{a}^*$ represents the initial guess of the kinematic variables, which is $\mathbf{a}^* = \mathbf{0}$ for the convex case as considered here. The column matrix $d\mathbf{a}$ represents corrections to the initial guess. Similar to column matrix $\mathbf{f}$, the stiffness matrix is assembled from contributions of each beam in the lattice:

$$\mathbf{K} = \frac{\partial^2 E_{int}(\mathbf{a})}{\partial \mathbf{a}^2} = \sum_{i=1}^{b} \frac{\partial^2 E_i(\mathbf{a})}{\partial \mathbf{a}^2} = \sum_{i=1}^{b} \mathbf{K}_i, \tag{8}$$

where the components of $\mathbf{K}_i$ are given by:

$$(K_i)_{pq} = \frac{\partial^2 E_i}{\partial a_q \partial a_p}, \tag{9}$$

where p and q run over all components of $\mathbf{a}$.

After incorporating Neumann boundary conditions in $\mathbf{f}_{ext}$ and Dirichlet boundary conditions in $\mathbf{a}$ and partioning the system resulting from Eq. (7), the system can be solved.

Solving such a system is computationally exhaustive for large beam lattices for two reasons. First, if the number of n lattice nodes in the beam lattice is large, solving the $6n$ scalar equations resulting from Eq. (7) is computationally expensive. The second cause of large computational costs (i.e. large computation times) is the effort required to construct the governing equations in Eq. 7. The assembly procedure to construct the governing equations is computationally costly because all b beams of the entire lattice must be visited according to the sums present in Eq. (5) and (8).

3. QC approaches for beam lattices

The QC method (Tadmor et al., 1996a,b) aims to overcome these two causes of large computational efforts of direct lattice computations. First, QC frameworks propose to interpolate the kinematic variables to reduce the number of degrees of freedom (see the first step in Fig.2). In the subsequent step, the QC method proposes to select only a small number of all b lattice interactions to obtain an estimate of the governing equations, instead of visiting all b beams. Employing these two reduction steps may lead to associated errors (see Fig. 2), but if they are carefully employed the total error ($e(int + sum)$ in Fig. 2) is insignificant and an increase of computational efficiency of at least one order of magnitude is achievable.

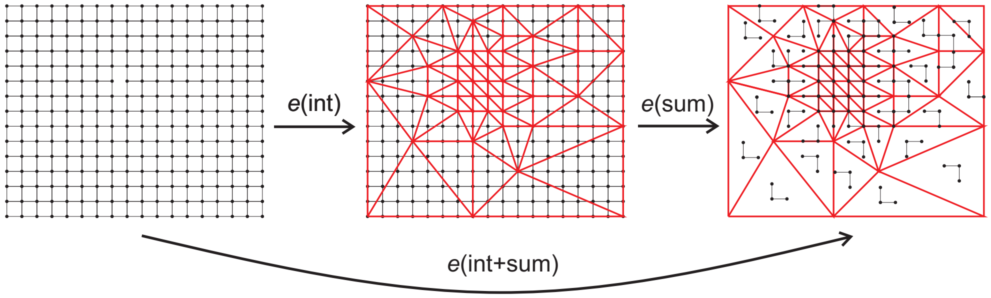

Figure 2: Schematic representation of the two reduction steps introduced in the QC method. In both reduction steps an error, e, may be introduced.

3.1. Interpolation of beam lattices

Interpolation of lattice variables (kinematic variables and sometimes also internal history variables (Beex et al., 2014b)) is employed in QC methodologies by selecting a small number of lattice points to represent the variables of the entire lattice. Therefore, these lattice points are often referred to as representative points or reppoints. Interpolation functions are defined in between the reppoints to interpolate the variables of the lattice points in between them. The used interpolation functions are similar to the shape functions used in finite element (FE) frameworks. This has the benefit that technologies developed in decades of FE research can rather straightforwardly be used in QC frameworks, e.g. adaptivity (Peerlings et al., 2008).

In domains with small fluctuations of the variables, the distance between the reppoints (i.e. the interpolation triangles) can be relatively large. If large fluctuations occur - e.g. around local events such as lattice defects and locally applied deformations - more reppoints are required in order to capture all fluctuations occurring in the lattice (see Fig. 2). In the limit, all lattice points are selected as reppoints, so that interpolation effectively does not occur. Regions in which all lattice points are selected as reppoints are fully resolved, which makes the QC method a true multiscale approach. After all, in regions of interest the small-scale (e.g. meso-scale or micro-scale) discrete lattice model is fully resolved, whereas in the rest of the domain the lattice model is interpolated and thus effectively homogenised.

Only linear interpolation is used so far in QC approaches, but for beam lattices higher order interpolation functions are useful, as shown below. As a result of the use of higher order interpolation, more triangle nodes (reppoints) are required to span the interpolation triangles, but if higher order interpolation functions are used, it cannot be guaranteed that all the triangle nodes are located on top of lattice nodes. As will be shown below however, numerical issues that arise from this can be overcome by relatively straightforward means.

Due to interpolation the kinematic variables of all lattice nodes are now expressed as follows:

$$\mathbf{a} \approx \bar{\mathbf{a}} = \mathbf{\Psi} \mathbf{a}_r, \tag{10}$$

where $\bar{\mathbf{a}}$ are the kinematic variables of all n lattice nodes in the interpolated (i.e. condensed) system, $\mathbf{\Psi}$ is the condensation matrix of size $6n \times 6r$ that contains the interpolation function evaluations at the locations of all n lattice nodes and $\mathbf{a}_r$ contains the $6r$ kinematic variables of the r triangle nodes.

As a consequence of the interpolation, the minimization has to be performed with respect to $\mathbf{a}_r$, instead of $\mathbf{a}$:

$$\mathbf{a}_r = \underset{\mathbf{a_r}^*}{\operatorname{argmin}} \, E_{tot}(\mathbf{a}_r^*). \tag{11}$$

By substitution of Eq. (10) in Eq. (7), the governing equations of the condensed lattice are expressed as follows:

$$\delta \mathbf{a}_r^T (\mathbf{\Psi}^T \mathbf{f}(\mathbf{a}_r^*) + \mathbf{\Psi}^T \mathbf{K} \mathbf{\Psi} d\mathbf{a}_r) = \delta \mathbf{a}_r^T \mathbf{\Psi}^T \mathbf{f}_{ext} \qquad \forall \delta \mathbf{a}_r, \tag{12}$$

where the condensed counterparts of $\mathbf{f}$ and $\mathbf{K}$ can be identified as $\mathbf{\Psi}^T \mathbf{f}$ and $\mathbf{\Psi}^T \mathbf{K} \mathbf{\Psi}$, respectively. We leave $\mathbf{f}_{ext}$ out of consideration in the derivation from here onwards.

In some of the frameworks proposed below, the order of the interpolation used for the nodal displacements is different from the order of the interpolation used for the nodal rotations. Consequently, the triangle nodes of the interpolation triangles for the nodal displacements are not necessarily the same as those of the interpolation triangles for the nodal rotations. Therefore, the total of r triangle nodes is split in a part used for the displacements, r_u, and in a part used for the rotations, r_θ - although some of the triangle nodes are used to interpolate the displacements as well as the rotations. In correspondence to this differentiation, Eq. (10) can be reformulated as follows, if we still use $\mathbf{a} = [\mathbf{U}^T \, \mathbf{\Theta}^T]^T$ for ease of notation:

$$\bar{\mathbf{a}} = \begin{bmatrix} \bar{\mathbf{U}} \\ \bar{\mathbf{\Theta}} \end{bmatrix} = \begin{bmatrix} \mathbf{\Psi}_u & 0 \\ 0 & \mathbf{\Psi}_\theta \end{bmatrix} \begin{bmatrix} \mathbf{U}_{r_u} \\ \mathbf{\Theta}_{r_\theta} \end{bmatrix}, \tag{13}$$

where $\bar{\mathbf{U}}$ and $\bar{\mathbf{\Theta}}$ are the condensed displacements and rotations of the interpolated lattice, respectively, and $\mathbf{\Psi}_u$ (of size $3n \times 3r_u$) and $\mathbf{\Psi}_\theta$ (of size $3n \times 3r_\theta$) are the condensation matrices associated with the interpolation of the displacements and rotations, respectively. The $3r_u$ displacements of the r_u triangle nodes spanning the interpolation triangles for the displacements are represented by $\mathbf{U}_{r_u}$ and the $3r_\theta$ rotations of the r_θ triangle nodes spanning the interpolation triangles for the rotations are presented by $\mathbf{\Theta}_{r_\theta}$.

3.1.1. Linear interpolation of the displacements and the rotations

The first QC scheme for beam lattices proposed here interpolates the displacements as well as the rotations linearly. Linear interpolation of both types of kinematic variables has the advantage that this is in correspondence with most previous QC frameworks (Tadmor et al., 1996a,b; Miller et al., 1998; Knap and Ortiz, 2001; Miller and Tadmor, 2002; Eidel and Stukowski, 2009; Beex et al., 2011, 2013b) and that possibly several technologies yet developed for QC methods can rather directly be employed. Examples are summation rules that specifically focus on linear interpolation, such as the central summation rule (Beex et al., 2013b) which is similarly accurate for the mixed formulation QC framework used by Beex et al. (2014b). Another advantage is that the same triangle nodes can be selected for both interpolations ($r = 2r_u$, $r_u = r_\theta$ and $\mathbf{\Psi}_u = \mathbf{\Psi}_\theta$). Linear interpolation of the displacements and the rotations also ensures that the discrete beam lattice is automatically fully resolved in domains of interest that are required to be fully resolved (see the left image of Fig. 3).

In most QC methodologies, the transition of the size of interpolation triangles from fully resolved domains to coarse domains is gradual as can be seen in Fig. 2 and in the left image of Fig. 3. However, QC results in studies such as the one by Beex et al. (2011) show that a high accuracy in fully resolved domains can best be achieved by enlarging the fully resolved domains and not by decreasing the size of the triangles in coarse domains (if one desires to keep the computational gain as large as possible). Global responses such as force-displacement responses remain relatively unaffected in all cases (Beex et al., 2014a).

Thus, previous studies indicate that it is computationally most convenient to coarsen the triangulation as much as possible outside the fully resolved domain. Acting on this observation, we not only investigate the efficiency and accuracy of triangulations that are traditionally used in QC methodologies, which gradually coarsen away from fully resolved domains, but in the following section we also investigate the possibilities in terms of accuracy and efficiency for non-conforming triangulations that use large triangles in the entire coarse domain without gradual coarsening, as shown on the right in Fig. 3. The kinematic variables of the triangle nodes at the internal interface in these frameworks are interpolated using the coarse triangles (see the right image in Fig. 3 again).

3.1.2. Cubic interpolation of the displacements and quadratic interpolation of the rotations

The Hermite interpolation that is traditionally used for a linear elastic beam (as well as in this study, see Appendix A) means that the local beam deflections (the displacements orthogonal to the beam's central axis) are interpolated in a cubic fashion and that the (non-torsional) local beam rotations are interpolated in a quadratic fashion. After all, the local rotations are defined as the derivatives of the local beam deflections (see Appendix A). Consequently, if several beam elements are used to discretise one single rod, the nodal deflections may show a cubic profile over the rod's central axis and the nodal rotations may show a quadratic profile.

To be able to capture these cubic displacements and quadratic rotations in the lattice nodes, which are especially important for out-of-plane deformations, a second QC framework is proposed here that interpolates the nodal displacements cubically and the nodal rotations quadratically (using ten and six nodes per triangle respectively, see Fig 4). In contrast to QC frameworks with linear interpolation, the use of interpolations of different orders ensures

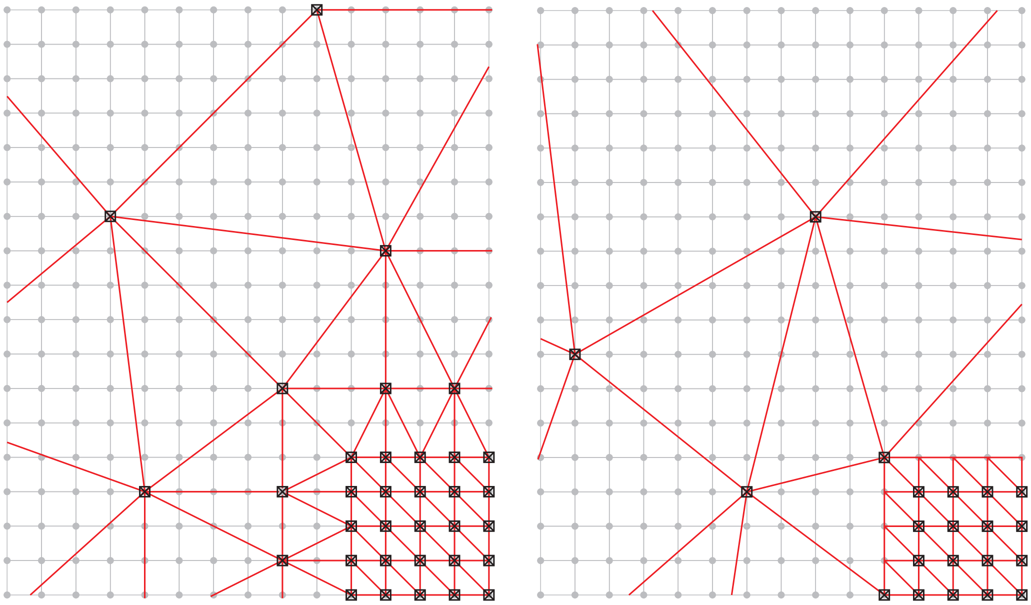

Figure 3: Schematic representation of linear interpolation triangles superimposed on the planar beam lattice. Left: a conforming triangulation, right: a non-conforming triangulation. In the bottom right corners of both images fully resolved regions can be seen. Black squares represent triangle nodes that interpolate the displacements and black crosses represent triangle nodes used to interpolate the rotations.

that two seperate sets of reppoints must be used to span the cubic triangles and the quadratic triangles. Furthermore, it is possible that triangle nodes are not located on top of lattice points - making the term 'reppoints' not very appropriate for these schemes (see Fig. 4).

The cubic and quadratic interpolation of the nodal displacements and nodal rotations forms a problem in fully resolved domains. The cause is that only the corner nodes of the triangles are located on top of all lattice points in these domains. Hence, the number of triangle nodes (i.e. degrees of freedom) is too large to be adequately governed by the underlying beam lattice, leading to ill-posed systems. To overcome this numerical issue, linear interpolation of the displacements and rotations is used in fully resolved regions of the QC schemes with non-conforming triangulations. This means that in these domains effectively no interpolation takes place and that the beam lattice is truly fully resolved, as is the case for QC frameworks that use linear interpolation of both the displacements and the rotations.

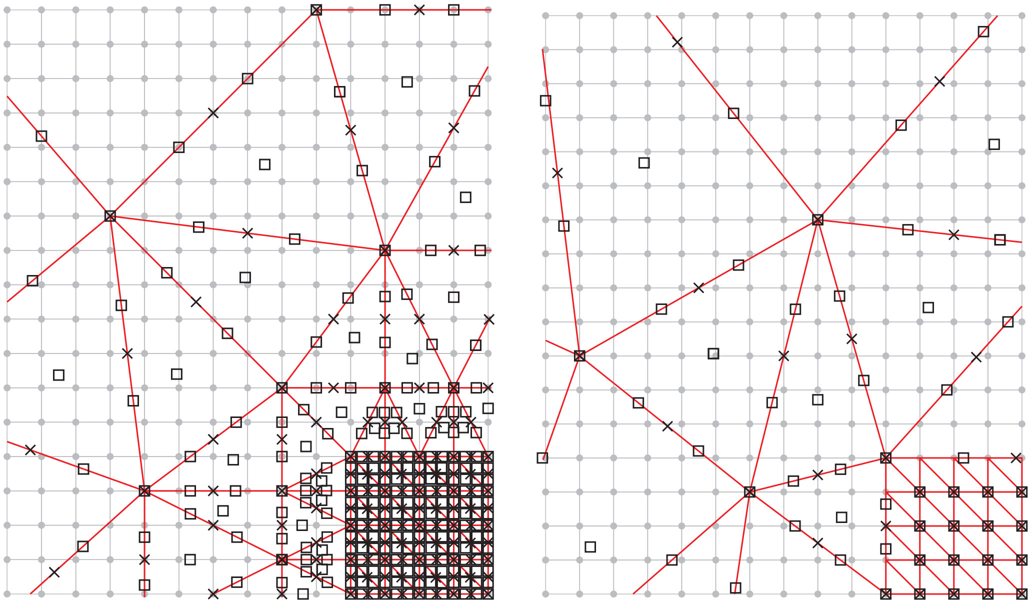

Figure 4: Schematic representation of cubic interpolation triangles and quadratic interpolation triangles superimposed on the planar beam lattice. Left: a conforming triangulation, right: a non-conforming triangulation. In the bottom right corners of both images fully resolved regions can be seen. Black squares represent triangle nodes that interpolate the displacements and black crosses represent triangle nodes used to interpolate the rotations.

The same numerical issue takes place just outside fully resolved domains for the conforming triangulations traditionally used in QC frameworks, since outside the fully resolved regions also more kinematic variables are present in the imposed triangles than in the underlying beam lattice. Also this will lead to ill-posed systems if left untreated, but in contrast to fully resolved domains the difficulty is that a priori it is substantially more difficult to assess in which triangles which degrees of freedom are not governed by the underlying beams. Even if it is possible to determine this for each triangle (a posteriori), individual interpolation functions need to be defined for a significant number of triangles, which makes the implementation more complex and compromises the efficiency of the overheads.

In this study, we will use an algebraic regularisation of the linear system arising from this type of interpolation, so that the separate formulation of individual interpolation functions is effectively avoided. These systems are rank defficient: the nullspace of the associated matrices may contain interpolation modes that are not energetically controlled by the underlying lattice. the generalized mimimal residual (GMRES) algorithm (Saad and Schultz, 1986) can provide a least-mean-square solution to such systems, as shown by Brown and Walker (1997), theorem 2.4. As our systems are consistent (the right hand-side of the system belongs to the range of the matrix), symmetric (which implies that the rank of the matrix is equal to the rank of its transpose) and the chosen initial guess is zero, GMRES delivers the pseudo-inverse solution before breaking by rank defficiency of the Krylov subspace.

This numerical issue is not present for non-conforming triangulations that are also investigated for the higher order interpolations in the subsequent section (see the right image in Fig. 4). A condition for this is that interpolation triangles are not allowed to be smaller than a particular size, but for the cases presented below no problems were observed, whilst the triangles are significantly small (as can be observed on the right in Fig. 4). In the fully resolved domains, the triangles are always of the same size and only the corner nodes are located on top of lattice nodes (as described above). Since in those domains the size and orientation of the triangles are a priori known, this can straightforwardly be implemented by linearly interpolating the displacements and rotations in these regions (as described above as well).

Although the number of scalar equations resulting from Eq. (12) for the condensed beam lattice is only $6r$, compared to the $6n$ scalar equations resulting from Eq. (7) for the direct beam lattice, still all b beams of the lattice have to be visited to assemble the governing equations. This extensive assembly procedure significantly compromises the use of direct (and interpolated) beam lattices defined at small scales for engineering scale applications.

3.2. Summation

The remedy proposed in QC methodologies is to select only a small number of s sampling interactions (i.e. beams) to approximate the governing equations, instead of visiting all b beams. The assembly of the approximated governing equations is obviously only more efficient if $s \ll b$. The sampling interactions (stored in subset S) are selected from all interactions ($S \subseteq B$). Each sampling interaction is used to sample the lattice interactions of the same type in its vicinity. The number of interactions that sampling interaction i represents is accounted for in its weight factor w_i (including sampling interaction i itself). To guarantee that in fully resolved regions the beam lattice is truly fully resolved, all interactions in the fully resolved regions are selected as sampling interactions that only represent themselves ($w_i = 1$).

Since the kinematic variables (i.e. the degrees of freedom) of the summed, condensed beam lattice remain the same as the for the condensed beam lattice, the minimization remains with respect to the degrees of freedom of the condensed lattice ($\mathbf{a}_r$). As a result of summation however, the construction of the internal potential energy changes to:

$$E_{int}(\mathbf{a}) \approx \bar{E}_{int}(\mathbf{a}_r) \approx \tilde{\bar{E}}_{int}(\mathbf{a}_r) = \sum_{i \in S} w_i \bar{E}_i(\mathbf{a}_r), \tag{14}$$

where $\bar{E}_{int}$ refers to the internal potential energy of the condensed beam lattice and $\tilde{\bar{E}}_{int}$ refers to the internal potential energy of the summed, condensed beam lattice. As a consequence, Eq. (12) is recast into the following expression:

$$\delta \mathbf{a}_r^T \left(\tilde{\bar{\mathbf{f}}}(\mathbf{a}_r^*) + \tilde{\bar{\mathbf{K}}} d\mathbf{a}_r \right) = \delta \mathbf{a}_r^T \tilde{\bar{\mathbf{f}}}_{ext} \qquad \forall \delta \mathbf{a}_r, \tag{15}$$

where $\tilde{\bar{\mathbf{f}}}$ and $\tilde{\bar{\mathbf{K}}}$ are the summed, condensed counterparts of $\mathbf{f}$ and $\mathbf{K}$ in Eq. (7), respectively. They can be determined as follows:

$$\tilde{\bar{\mathbf{f}}}(\mathbf{a}_r) = \frac{\partial \tilde{\bar{E}}_{int}(\mathbf{a}_r)}{\partial \mathbf{a}_r} = \sum_{i \in S} w_i \mathbf{\Psi}^T \frac{\partial E_i(\mathbf{a})}{\partial \mathbf{a}} = \sum_{i \in S} w_i \mathbf{\Psi}^T \mathbf{f}_i(\mathbf{a}), \tag{16}$$

$$\tilde{\bar{\mathbf{K}}} = \frac{\partial^2 \tilde{\bar{E}}_{int}(\mathbf{a}_r)}{\partial \mathbf{a}^2} = \sum_{i \in S} w_i \mathbf{\Psi}^T \frac{\partial^2 E_i(\mathbf{a})}{\partial \mathbf{a}^2} \mathbf{\Psi} = \sum_{i \in S} w_i \mathbf{\Psi}^T \mathbf{K}_i \mathbf{\Psi}. \tag{17}$$

The components of $\mathbf{f}_i$ and $\mathbf{K}_i$ are still given by Eq. (6) and (9), respectively.

The selection of the sampling interactions, the computation of their weight factors and the manner in which they are treated (locally or nonlocally) are defined in a summation rule. In literature a number of summation rules are proposed which all have their specific aim (Tadmor et al., 1996a,b; Miller et al., 1998; Knap and Ortiz, 2001; Miller and Tadmor, 2002; Eidel and Stukowski, 2009; Gunzburger and Zhang, 2010; Zhang and Gunzburger, 2010; Beex et al., 2011, 2013b). A common point is that they all try to accomplish that the condensed potential energy approximates the summed, condensed total potential energy as accurately as possible ($\bar{E}_{tot} \approx \tilde{\bar{E}}_{tot}$) with a minimum of sampling points/interactions in order to increase the computational efficiency as much as possible. However, all previously proposed summation rules focus on linear interpolation for atomistic lattices and are not aimed at mixed interpolations, higher order interpolations and structural lattice models as is the case in this study. Only the summation rules defined by Beex et al. (2011) and Beex et al. (2013b) were used for structural lattice models and the summation rule defined by Beex et al. (2013b) was used in the study of Beex et al. (2014b) for a structural lattice model in a mixed QC method.

3.2.1. Summation rules for higher order interpolation

The summation rule of Beex et al. (2011) developed QC frameworks with linear interpolation for instance, is based on an exact understanding of how the interpolation triangulation influences the potential energy of the (condensed) lattice. If higher interpolation functions are used for the kinematic variables however, it is far from trivial how the potential energy of the interpolated lattice is exactly governed by the interpolation. Therefore, the sampling interactions are selected near Gaussian quadrature points (GQPs) as used in FE technologies. This was previously proposed by Gunzburger and Zhang (2010) and Zhang and Gunzburger (2010), and to the best of the authors' knowledge only applied to one dimensional chains of atoms. Although for higher interpolation the lattice interactions that cross triangle edges possibly have a unique potential energy, similar to frameworks with linear interpolation, they are not selected as discrete sampling interactions to benefit the computational efficiency.

Since cubic interpolation of the displacements is used and quadratic interpolation of the rotations, the number of sampling interactions must be such that the internal potential energy due to the cubic interpolation of the displacements is accurately captured. In that case, the condensed internal potential energy is expected to be accurately captured to deal with the quadratic interpolation of the rotations as well.

Based on the cubic interpolation of the displacements, one might expect that four GQPs are sufficient according to FE technologies. Because one of these four GQPs is located exactly on top of the central triangle node used for the cubic interpolation of the displacements (see Appendix B) and because the sampling interactions are never exactly located on top of the GQPs however (see Fig. 5), the use of four GQPs leads to rather inaccurate results.

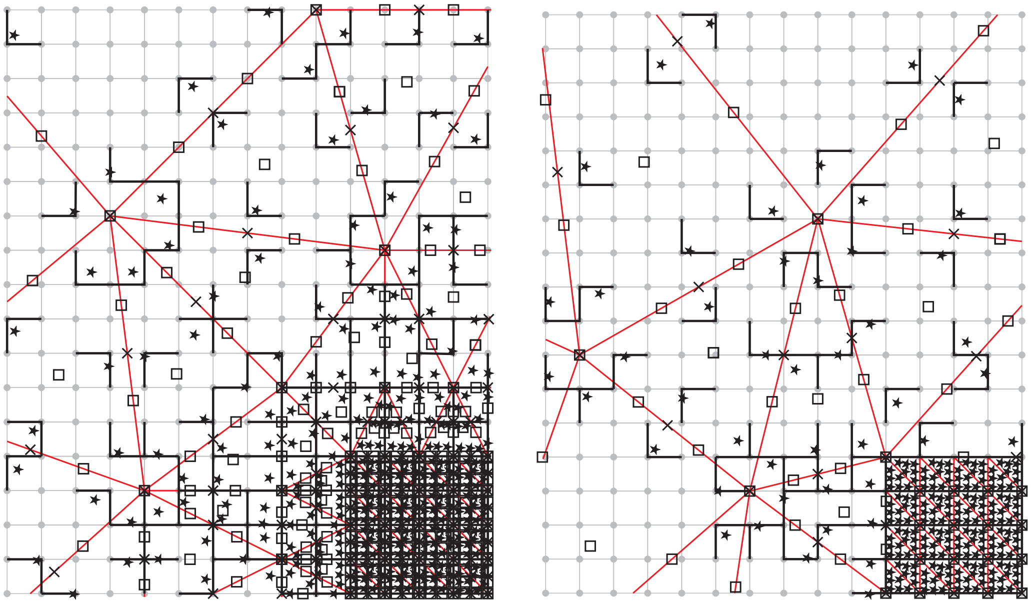

Figure 5: Schematic representation of the QC frameworks using cubic interpolation of the displacements and quadratic interpolation of the rotations and a summation rule based on the use of six Gaussian quadrature points per triangle applied to the planar beam lattice. Left: a conforming triangulation, right: a non-conforming triangulation. In the bottom right corners of both images fully resolved regions can be seen. Black squares represent triangle nodes that interpolate the displacements and black crosses represent triangle nodes used to interpolate the rotations. Black beams represent sampling beams. Black stars represent the locations of GQPs.

For this reason, the use of six, seven, nine and twelve GQPs are only investigated in the following section. The weight factor w_i of sampling interaction i is based on the weights of the GQP as used in FE technologies, w_{GQP}, as follows:

$$w_i = w_{GQP} b_{tr/T}, \tag{18}$$

where $b_{tr/T}$ is the total number of beams of the same type (horizontal or vertical) as sampling interaction i in the considered triangle. Hence, two sampling interactions, each with a unique weight factor, are selected per GQP (see Fig. 5). The locations and weights of the GQPs as used in this study can be found in Appendix A, which are adopted from Hughes (1987).

In case sampling interaction i is used for multiple GQPs, possibly in another triangle, the weight factors of this interaction is obviously determined by multiple weights and beams per triangle (w_{GQP} and $b_{tr/T}$). This leads in the limit of the fully resolved domains exactly to the fully resolved beam lattice as desired, i.e. $w_i = 1$ in these domains. Hence, the part of the implementation that accounts for the summation rule treats each interpolation triangle in the same manner, resulting in a minimum of implementation efforts.

4. Performance study

In this section, the accuracy and computational efficiency of the different QC frameworks are compared with each other. The accuracy and computational efficiency of the QC frameworks are based on the direct lattice computations. Three multiscale problems are used for the comparisons.

4.1. Description of the three test cases

For all three test cases a planar beam lattice is used of 70 × 50 square unit cells in horizontal (X-)direction and vertical (Y-)direction, respectively. The properties of the Euler-Bernoulli beams are given in Table 1. A single defect is included in the beam lattice by removing the horizontal beam on the right-hand side of the central lattice point. Consequently, 3621 lattice nodes (21,726 DOFs) and 7119 beams are present. The lattice is rather small so that the full lattice computations can be performed. As a result of the limited size of the lattice however, the computational gain reported below is small and larger computational efficiencies can easily be achieved for larger models using QC approaches (Beex et al., 2011, 2014a).

Table 1: The geometrical and material properties of the beams in the lattice. The same symbols are used as in Appendix A.

L [m]	1
t [m]	0.1
h [m]	1
Y [Pa]	1,000
ν [-]	0.3

In the first test case, the beam lattice is subjected to in-plane uniaxial deformation in the horizontal (X-)direction, as shown on the left in Fig. 6. This test case is two-dimensional (2D) and the displacements in the Z-direction and the rotations around the X- and Y-axes of all lattice nodes (triangle nodes in the QC models) are suppressed. The displacements and rotations of all lattice points (triangle nodes in the QC computations) on all four model edges are prescribed. The maximum prescribed horizontal displacement, present on the right model edge, equals $1m$. The horizontal displacements of the lattice nodes on the other model edges are such that uniform in-plane uniaxial deformation in the horizontal direction occurs if the lattice defect is not present. All other kinematic variables of the lattice nodes on the model edges are suppressed (i.e. they equal zero).

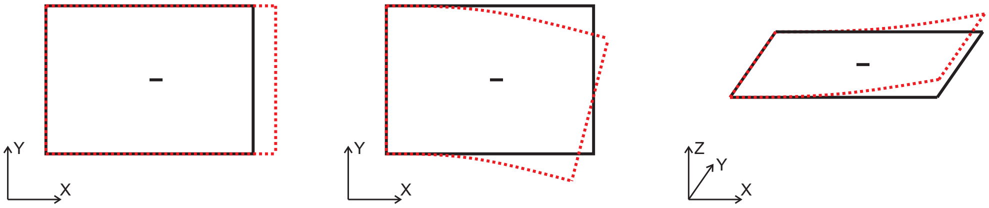

Figure 6: Schematic representation of the three numerical examples including a lattice defect: in-plane uniaxial deformation (left), in-plane bending (center) and out-of-plane bending (right).

The second test case is also fully 2D. Hence, in this case the displacements in the Z-direction and the rotations around the X- and Y-axes of all lattice nodes are also suppressed. In this numerical example, in-plane bending around the Z-axis is enforced by prescribing the kinematic variables of all lattice points on the four model edges (see the center image in Fig. 6). The applied bending radius equals $1000m$ and the center of the bending circle is located at the cartesian coordinates ($0m$, -$975m$, $0m$), if the origin of the global cartesian coordinate system spanned by the X-, Y- and Z-axes is located in the left bottom corner of the model.

The third numerical example is three-dimensional (3D) and considers out-of-plane deformation (see the right image in Fig. 6). All kinematic variables of the lattice nodes on the left model edge are constrained (i.e. they are set to zero), whilst the displacements in Z-direction of the lattice nodes on the right model edge are given a value of $1m$. All other kinematic variables of the lattice are free, as are those of the lattice nodes on the right model edge.

4.2. Reference results

In this subsection, the results of the three test cases are described that form the reference results for the QC frameworks. The reference results are established using the direct computations and consist of the absolute kinematic variables as well as the 'relative' kinematic variables. These relative kinematic variables are the kinematic variables relative to the test cases without a lattice defect and are a measure for the fluctuation induced by the single lattice defect.

The results computed with the full beam lattice serve as the reference results for the QC models, since these are the results QC frameworks aim to approach as accurately as possible. The deformed lattice computed by the

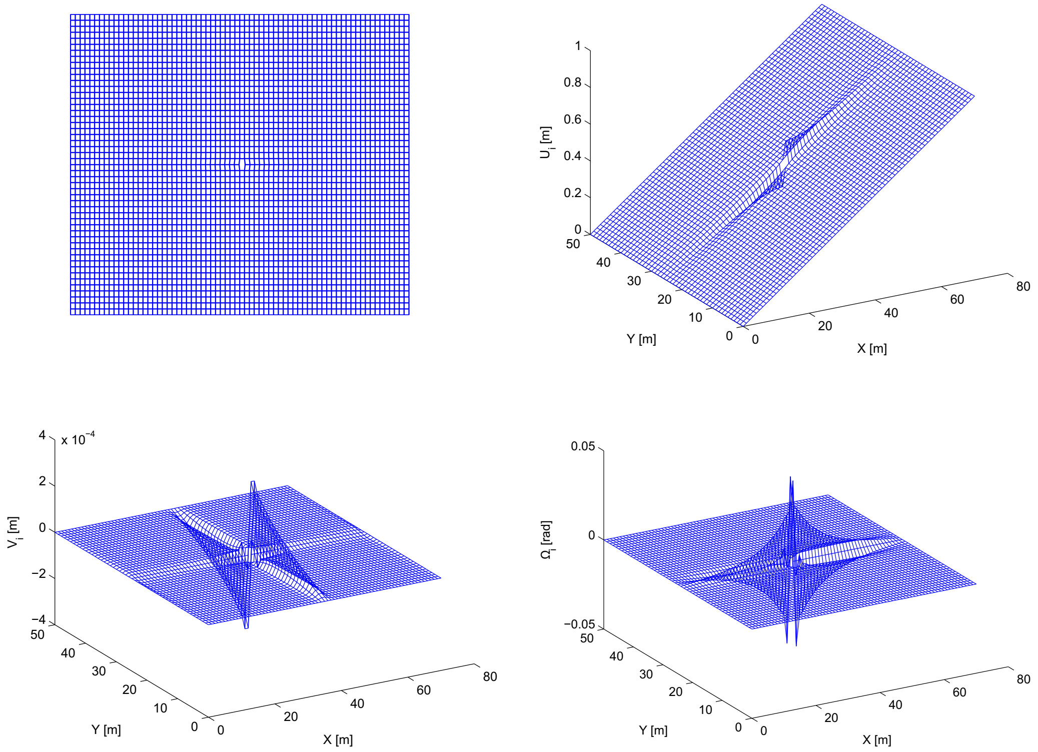

Figure 7: The results predicted by the direct lattice computation for in-plane uniform deformation in horizontal direction: the total deformation (top-left), the horizontal displacements of all lattice points, U_i (top-right), the vertical displacements of all lattice points, V_i (bottom-left) and the rotations around the Z-axis of all lattice points, Ω_i (bottom-right).

direct lattice computation for the first test case in which uniaxial horizontal deformation is prescribed are presented in the top-left image of Fig. 7. Significant fluctuations can be observed around the lattice defect.

The horizontal (in X-direction) and vertical (in Y-direction) displacements of the lattice nodes and the rotations around Z-axis are separately presented in Fig. 7 as well. The horizontal displacement components clearly show a linear function in the X-direction with a relative fluctuation field that is caused by the lattice defect. The vertical displacements and the rotations around the Z-axis only show relative fluctuation fields caused by the lattice defect.

The relative fluctuation fields caused by the lattice defect can be determined by incorporating the results predicted by the direct lattice computation without a lattice defect and the error based on this relative fluctuation field will a more stringent error measure than the error based on the absolute displacements (formulated below). The relative fluctuation field can be determined as follows:

$$\mathbf{a}^{rel} = \mathbf{a} - \mathbf{a}^{nold}, \tag{19}$$

where $\mathbf{a}^{nold}$ are the computed kinematic variables in the case where no lattice defect is present and $\mathbf{a}^{rel}$ are the kinematic variables that express the relative difference between the kinematic variables for the computations with and without lattice defect.

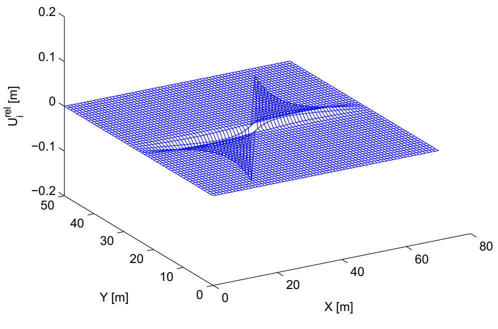

Figure 8: The relative horizontal displacements, U_i^{rel}, predicted with the direct lattice computation for in-plane uniform deformation in horizontal direction.

If the relative horizontal displacement components are extracted from $\mathbf{a}^{rel}$, Fig. 8 is obtained. This diagram clearly shows only the relative fluctuation of the horizontal displacements caused by the lattice defect. The relative vertical displacements and relative rotations around the Z-axis give the same result as the absolute vertical displacements and rotations around the Z-axis. Hence, the bottom diagrams in Fig. 7 present the absolute vertical displacements and absolute rotations around the Z-axis as well as the relative vertical displacements and relative rotations around the Z-axis.

The top-left image in Fig. 9 shows the deformed beam lattice for in-plane bending. Relative fluctuations are impossible to observe in this diagram. Also in the other three diagrams in Fig. 9 that separately present the hor-

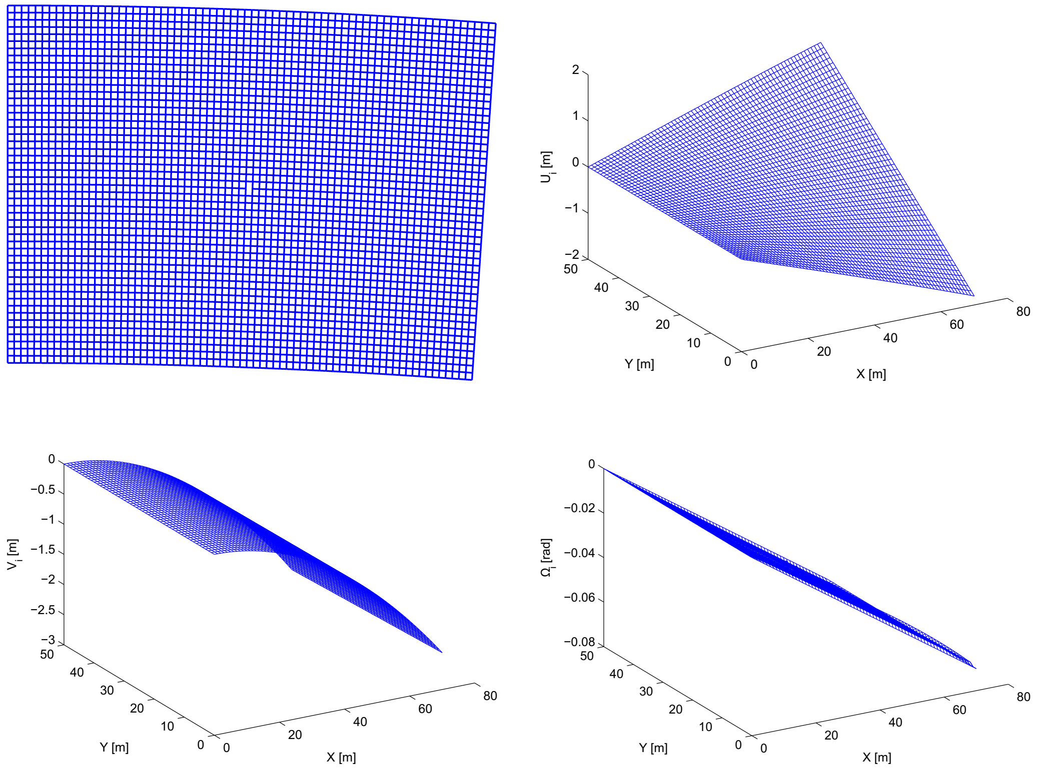

Figure 9: The results predicted with the direct lattice computation for in-plane bending: the total deformation (top-right), the horizontal displacements of all lattice points, U_i (top-right), the vertical displacements of all lattice points, V_i (bottom-left) and the rotations around the Z-axis of all lattice points, Ω_i (bottom-right).

izontal and vertical displacement components and the rotations around the Z-axis, do not show any relative fluctuations caused by the lattice defect.

The influence of the lattice defect on the results becomes clearly visible if the results predicted for in-plane bending without a lattice defect are subtracted according to Eq. (19). The relative horizontal and vertical displacements and relative rotations around the Z-axis are shown in Fig. 10. The influence of the lattice defect is rather similar to the relative kinematic variables in the case of in-plane uniaxial deformation, although the values are opposite.

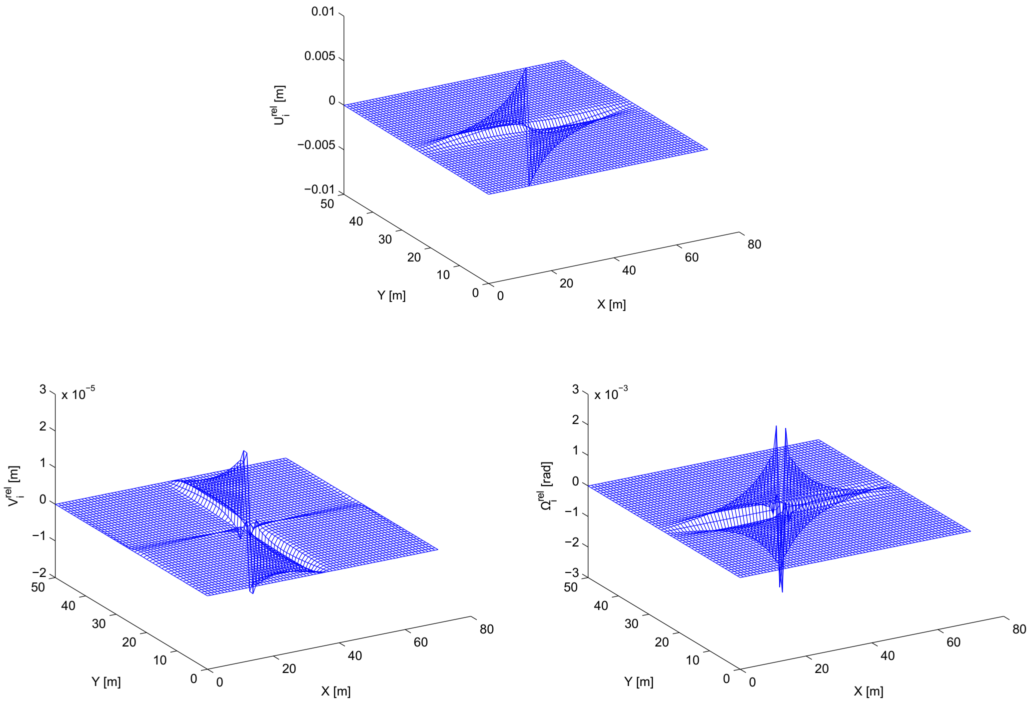

Figure 10: The relative horizontal displacements, U_i^{rel}, (top), the relative vertical displacements, V_i^{rel}, (bottom-left) and the relative rotations around the Z-axis, Ω_i^{rel}, (bottom-right) predicted with the direct lattice computation for in-plane bending.

The predicted deformation for the third case in which out-of-plane bending is applied is shown in the top-left image of Fig. 11. The influence of the lattice defect cannot be observed in the top-left image of Fig. 11. In the non-zero kinematic variables, the influence of the lattice defect can only be seen in the rotations around the X-axis in the bottom-left diagram of Fig. 11. The displacements in the Z-direction and the rotations around the Y-axis in the top-right and bottom-right diagram of Fig. 11, respectively, only show the global response.

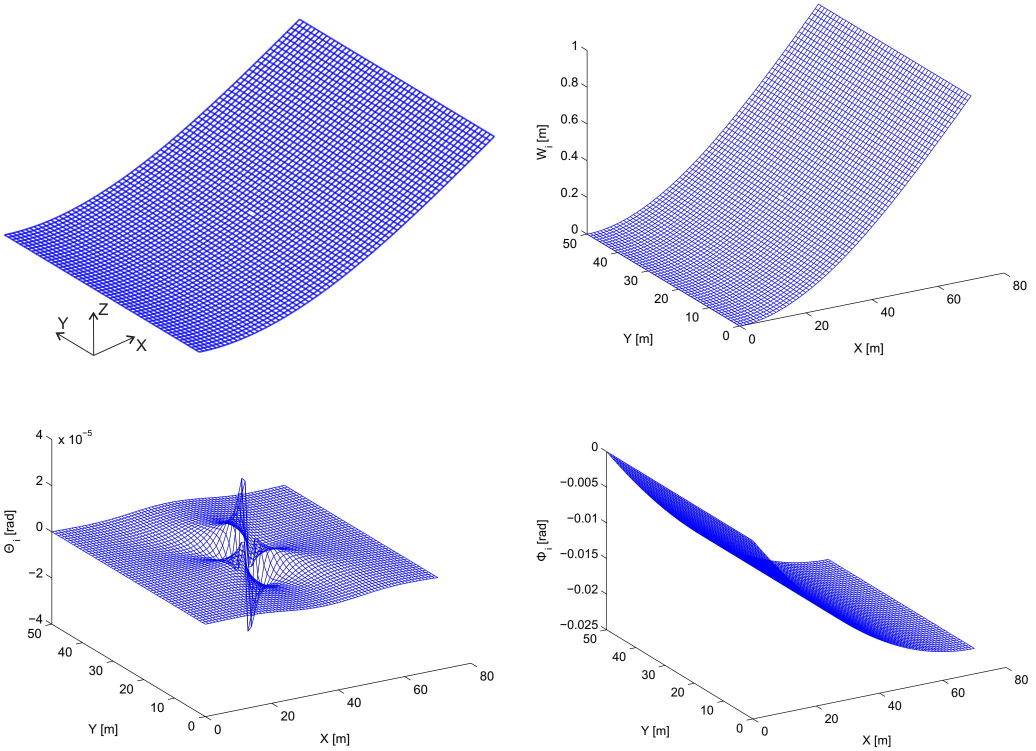

Figure 11: The results predicted with the direct lattice computation for out-of-plane bending: the total deformation (top-right), the displacements in Z-direction of all lattice points, W_i (top-right), the rotations around the X-axis of all lattice points, Θ_i (bottom-left) and the rotations around the Y-axis of all lattice points, Φ_i (bottom-right).

The influence of the lattice defect on the displacements in Z-direction and the rotations around the Y-axis can also in this case only be visualised if the results predicted by the computation without lattice defect are subtracted according to Eq. (19). The relative fluctuations of these two types of kinematic variables are shown in Fig. 12. The fluctuation fields are clearly different from the two 2D examples. Note that the absolute and relative rotations around the X-axis are the same and hence, they are both given by the bottom-left diagram in Fig. 11.

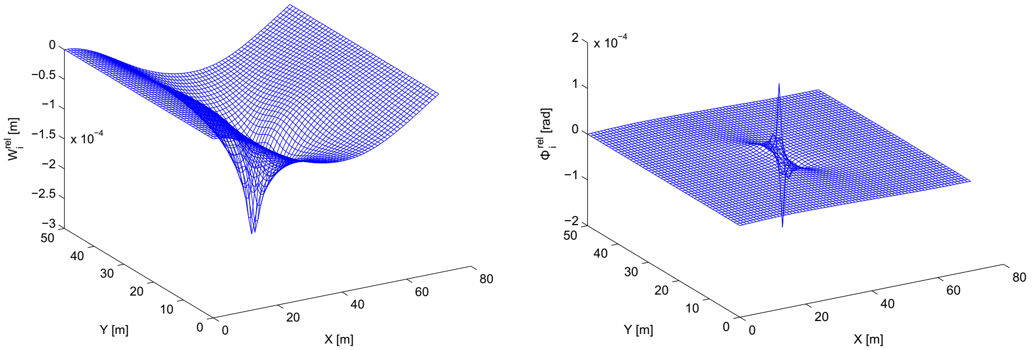

Figure 12: The relative displacements in Z-direction, W_i^{rel}, (left) and the relative rotations around the Y-axis, Φ_i^{rel}, (right) predicted with the direct lattice computation for out-of-plane bending.

4.3. Influence of interpolation

Before the full QC frameworks are considered, in which both interpolation and summation are present, the influence of interpolation alone is regarded. This means that no summation is present in the models considered in this subsection and that all lattice beams are used to construct the governing equations. The error due to summation (see Fig. 2) is zero and in this part we only focus on the error due to interpolation (see Fig. 2). In this subsection it will become clear that of the four investigated interpolation schemes, the one with non-conforming higher-order interpolations gives the most accurate results for all the three test cases.

As mentioned before, conforming and non-conforming interpolation triangulations are investigated in this study. In Fig. 13, the conforming triangulations are shown with fully resolved regions of 4, 6, 8, 10, 12 and 14 unit cells around the lattice defect. The coarse domain is automatically generated and the triangle nodes are subsequently moved to the nearest lattice nodes. This latter operation can lead to triangles with a zero area, which are removed. As a result of the automatic triangulation generation, it is possible that the fully resolved regions are not completely square. This is in contrast to the non-conforming triangulations shown in Fig. 14 and those considered by Beex et al. (2011, 2013b, 2014a).

In Fig. 15 some indicative results are shown for the first numerical example in which in-plane uniform deformation is considered. The two most important, general observations that can be made are that linear interpolation of the displacements and rotations gives almost as accurate results as cubic interpolation of the displacements and quadratic interpolation of the rotations for this loading case. Another observation is that the conforming triangulations are more accurate than the non-conforming triangulations. This is rather obvious since more DOFs are present in the conforming triangulations and that the additional DOFs are closely located to the fully resolved region. Below, this is considered in more detail.

In Fig. 16, the vertical displacements ($\bar{V}_i$) and the relative horizontal displacements ($\bar{U}_i^{rel}$) can be seen for the second numerical test case in which in-plane bending is applied. The vertical displacements predicted by cubic interpolation of the displacements and quadratic interpolation of the rotations are more accurate at first sight than if linear interpolation is used. This can also be seen for the relative horizontal displacements.

The relative rotations around Y-axis and the displacements in Z-direction are shown in Fig. 17 for the test case in which out-of-plane bending is applied. The results predicted by linear interpolation of all kinematic variables are clearly inaccurate, although the influence of the lattice defect can still be observed. The solution predicted by the conforming triangulation with cubic interpolation of the displacements and quadratic interpolation of the rotations is clearly inaccurate. This is most likely caused by the fact that the horizontal and vertical displacements and the rotations around the Z-axis are true DOFs in the computation, which are uncoupled to the other DOFs in Euler-Bernoulli beam theory. The results predicted by the non-conforming triangulations with cubic interpolation of the displacements and quadratic interpolation of the rotations are at first sight satisfyingly accurate.

To quantify the errors due to interpolation, two error measures are introduced. One error, e_{gl}, quantifies the error of the absolute values of the non-zero kinematic variables and e_{rel} measures the ability of the interpolation triangulation to capture the relative fluctuation induced by the lattice defect. For the 2D example in which uniform in-plane deformation is prescribed, the global error is defined as:

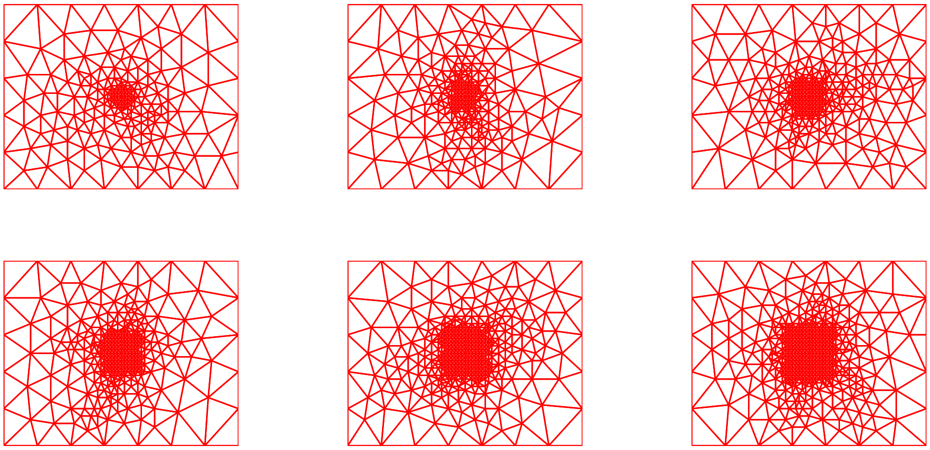

Figure 13: The six conforming triangulations with fully resolved regions of 4 (top-left), 6 (top-center), 8 (top-right), 10 (bottom-left), 12 (bottom-center) and 14 unit cells (bottom-right).

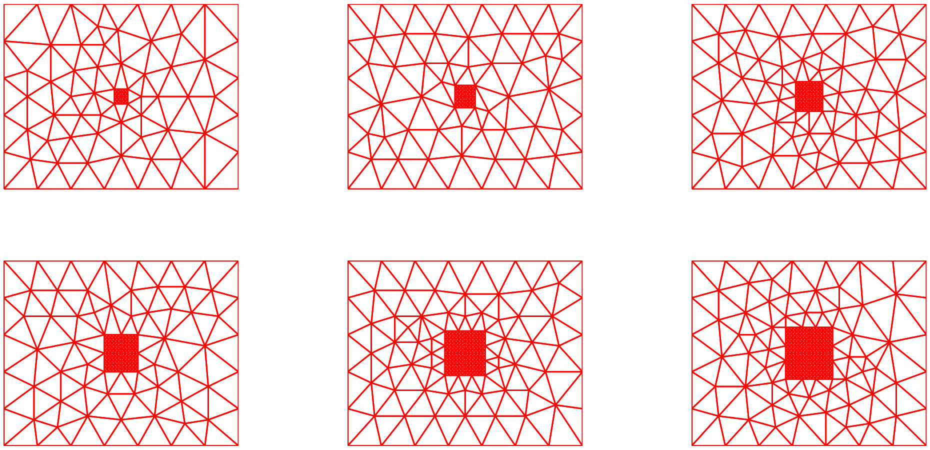

Figure 14: The six non-conforming triangulations with fully resolved regions of 4 (top-left), 6 (top-center), 8 (top-right), 10 (bottom-left), 12 (bottom-center) and 14 unit cells (bottom-right).

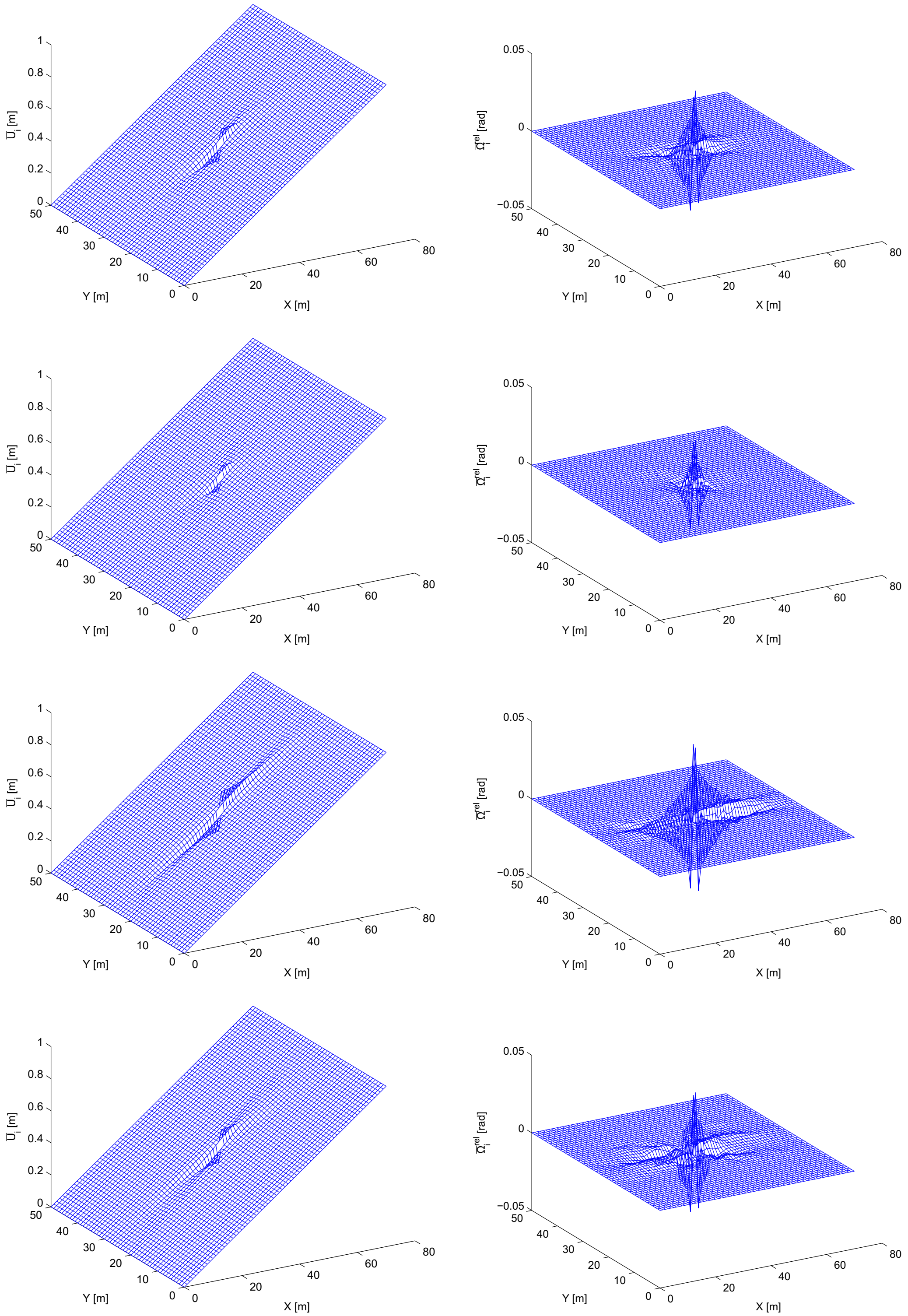

Figure 15: The horizontal displacements ($\bar{U}_i$) and the relative rotations around the Z-axis ($\bar{\Omega}_i^{rel}$), left and right, respectively, predicted for the first test case using the triangulations with a fully resolved region of 10 × 10 unit cells for linear interpolation of the displacements and rotations and a conforming triangulation (top), linear interpolation of the displacements and rotations and a non-conforming triangulation (second from top), cubic interpolation of the displacements and quadratic interpolation of the rotations and a conforming triangulation (second from bottom) and cubic interpolation of the displacements and quadratic interpolation of the rotations and a non-conforming triangulation (bottom).

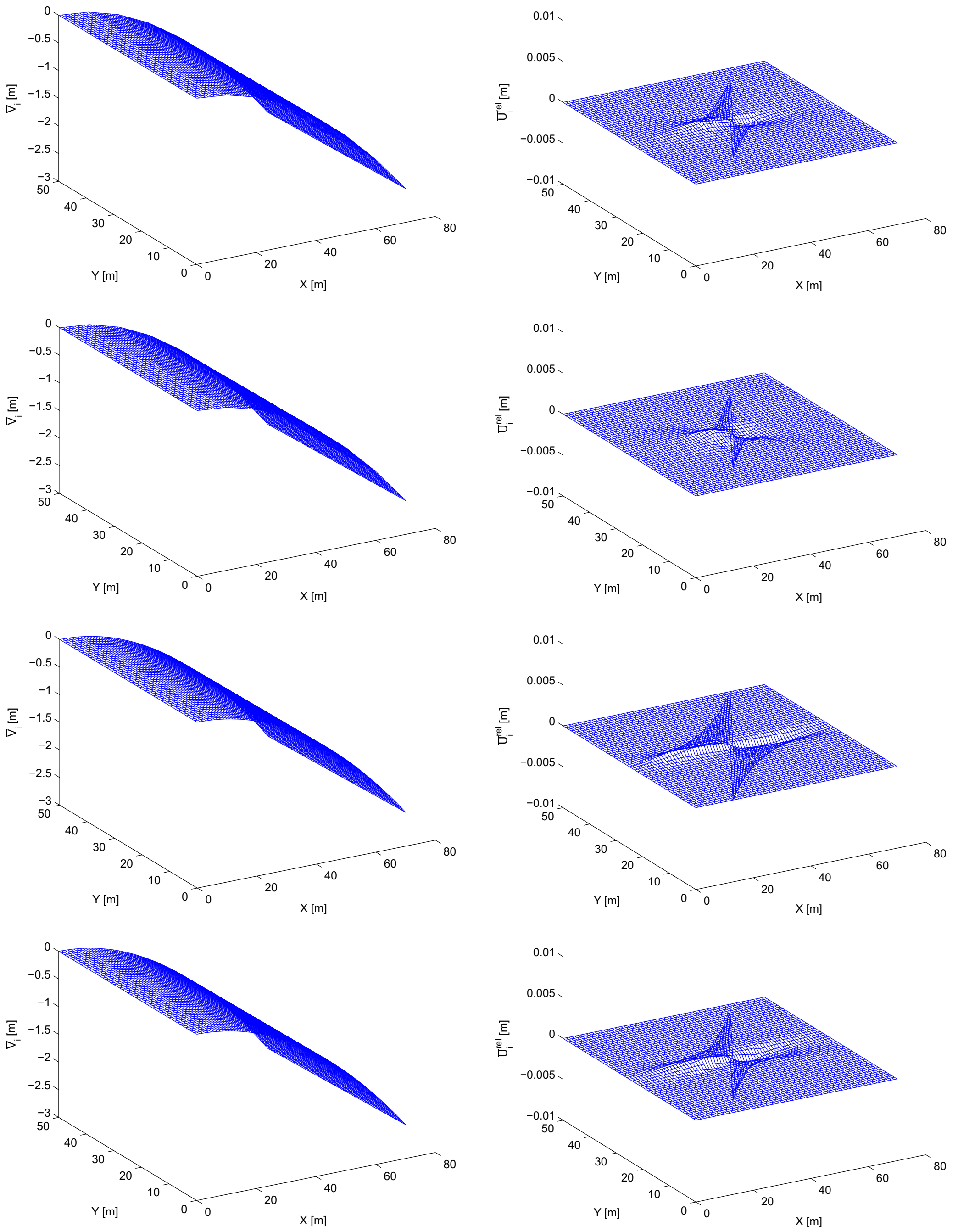

Figure 16: The horizontal displacements ($\bar{U}_i$) and the relative rotations around the Z-axis ($\bar{\Omega}_i^{rel}$), left and right, respectively, predicted for the second test case using the triangulations with a fully resolved region of 10 × 10 unit cells for linear interpolation of the displacements and rotations and a conforming triangulation (top), linear interpolation of the displacements and rotations and a non-conforming triangulation (second from top), cubic interpolation of the displacements and quadratic interpolation of the rotations and a conforming triangulation (second from bottom) and cubic interpolation of the displacements and quadratic interpolation of the rotations and a non-conforming triangulation (bottom).

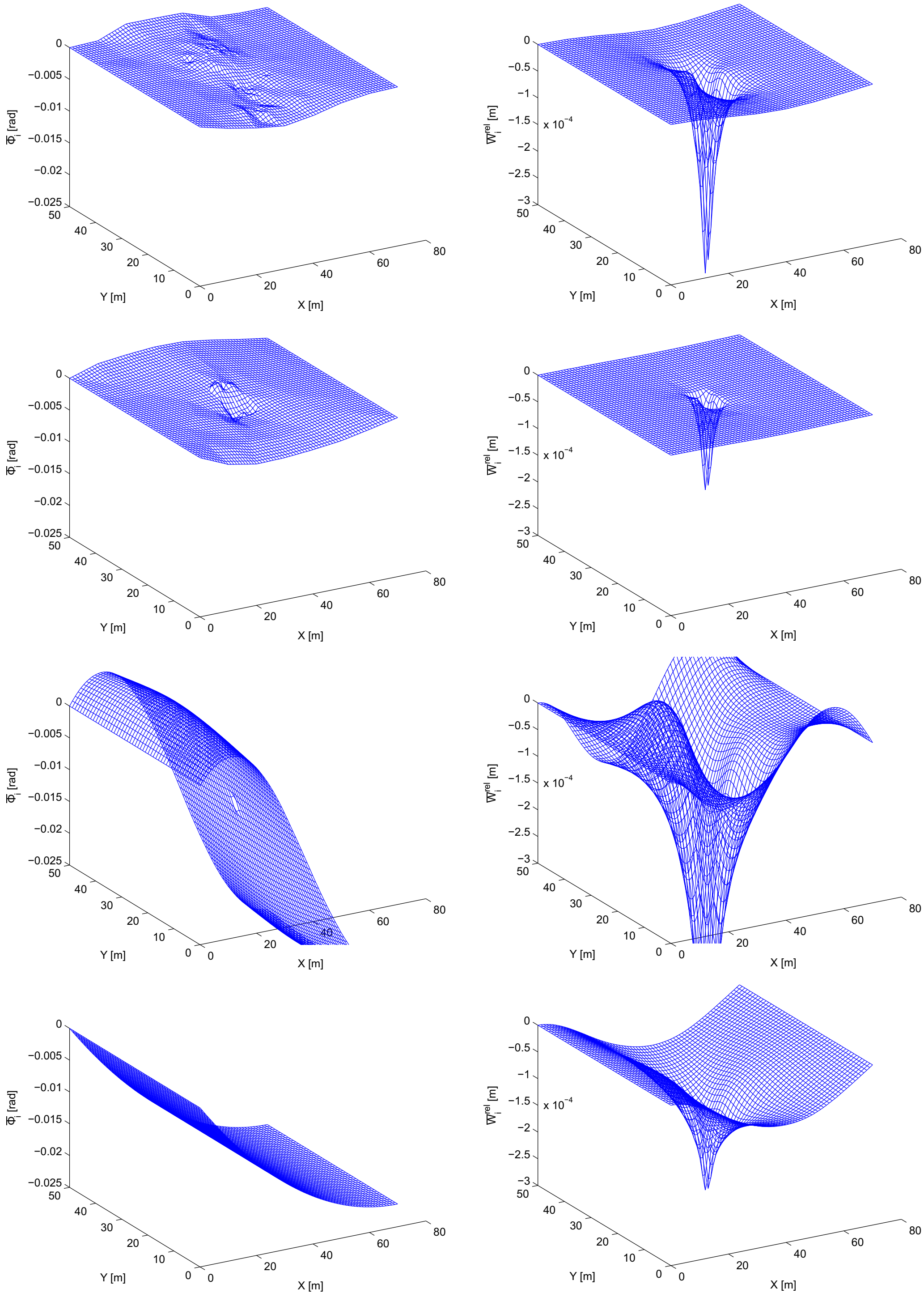

Figure 17: The horizontal displacements ($\bar{U}_i$) and the relative rotations around the Z-axis ($\bar{\Omega}_i^{rel}$), left and right, respectively, predicted for the third test case using the triangulations with a fully resolved region of 10 × 10 unit cells for linear interpolation of the displacements and rotations and a conforming triangulation (top), linear interpolation of the displacements and rotations and a non-conforming triangulation (second from top), cubic interpolation of the displacements and quadratic interpolation of the rotations and a conforming triangulation (second from bottom) and cubic interpolation of the displacements and quadratic interpolation of the rotations and a non-conforming triangulation (bottom).

$$e_{gl} = \sqrt{\frac{\sum_{i=1}^{n}(\bar{U}_i - U_i)^2}{\sum_{i=1}^{n}(U_i)^2}} \cdot 100\%, \tag{20}$$

and for the 2D example with in-plane bending it is defined as:

$$\begin{aligned} e_{gl} = \Bigg(&\frac{1}{3}\sqrt{\frac{\sum_{i=1}^{n}(\bar{U}_i - U_i)^2}{\sum_{i=1}^{n}(U_i)^2}} + \frac{1}{3}\sqrt{\frac{\sum_{i=1}^{n}(\bar{V}_i - V_i)^2}{\sum_{i=1}^{n}(V_i)^2}} + \\ &\frac{1}{3}\sqrt{\frac{\sum_{i=1}^{n}(\bar{\Omega}_i - \Omega_i)^2}{\sum_{i=1}^{n}(\Omega_i)^2}}\Bigg) \cdot 100\%, \end{aligned} \tag{21}$$

and finally for the 3D example as:

$$e_{gl} = \left(\frac{1}{2}\sqrt{\frac{\sum_{i=1}^{n}(\bar{W}_i - W_i)^2}{\sum_{i=1}^{n}(W_i)^2}} + \frac{1}{2}\sqrt{\frac{\sum_{i=1}^{n}(\bar{\Phi}_i - \Phi_i)^2}{\sum_{i=1}^{n}(\Phi_i)^2}}\right) \cdot 100\%, \tag{22}$$

where the bar on top of the type of kinematic variables refers to the results computed with the interpolation triangulations. By incorporating each kinematic variable in these and the following error measures with the same weight and neglecting the types of kinematic variables that are zero (or close to zero), the error measures become independent of the geometrical and material properties of the beam lattice (given in Table 1).

The relative errors - that measure the error of the relative fluctuation field caused by the single lattice defect - for the 2D examples are both defined as follows:

$$\begin{aligned} e_{rel} = \Bigg(&\frac{1}{3}\sqrt{\frac{\sum_{i=1}^{n}(\bar{U}_i^{rel} - U_i^{rel})^2}{\sum_{i=1}^{n}(U_i^{rel})^2}} + \frac{1}{3}\sqrt{\frac{\sum_{i=1}^{n}(\bar{V}_i^{rel} - V_i^{rel})^2}{\sum_{i=1}^{n}(V_i^{rel})^2}} + \\ &\frac{1}{3}\sqrt{\frac{\sum_{i=1}^{n}(\bar{\Omega}_i^{rel} - \Omega_i^{rel})^2}{\sum_{i=1}^{n}(\Omega_i^{rel})^2}}\Bigg) \cdot 100\%, \end{aligned} \tag{23}$$

and for the 3D example as:

$$e_{rel} = \left(\frac{1}{3}\sqrt{\frac{\sum_{i=1}^{n}(\bar{W}_i^{rel} - W_i^{rel})^2}{\sum_{i=1}^{n}(W_i^{rel})^2}} + \frac{1}{3}\sqrt{\frac{\sum_{i=1}^{n}(\bar{\Theta}_i^{rel} - \Theta_i^{rel})^2}{\sum_{i=1}^{n}(\Theta_i^{rel})^2}} + \frac{1}{3}\sqrt{\frac{\sum_{i=1}^{n}(\bar{\Psi}_i^{rel} - \Psi_i^{rel})^2}{\sum_{i=1}^{n}(\Psi_i^{rel})^2}}\right) \cdot 100\%. \quad (24)$$

The errors for the different interpolations are shown in Fig. 18 for the three numerical examples. They are shown as a function of the relative number of DOFs. The relative number of DOFs should be read in Fig. 18 as the solution space and not as a factor of computational burden. The reason is that although less DOFs are present than in the direct lattice computation, the computational time to solve the system may well be larger than the computational time to solve the direct lattice computation. The reason is the poor conditioning of the stiffness matrix for condensed (interpolated) systems that render relatively long computation times for iterative solvers. Preconditioning may avoid this, but it is not considered in this study. The true computational gain in QC methodologies (without preconditioning) thus stems from summation, i.e. the reduction in efforts to construct the governing equations. Hence, the computational time that is saved scales with the number of sampling interactions as reported by Beex et al. (2014a).

If we first consider the errors for the conforming triangulations using linear interpolation, it can be observed that the global and relative errors are sufficiently accurate for uniform in-plane deformation. The relative error reduces for the fully resolved regions to approximately 30% for the triangulation with a fully resolved region of 14 × 14 unit cells. It is expected however that this error remains significant for a further increase of the size of the fully resolved region, because the influence of the single lattice defect is significantly non-local as can be seen in Fig. 7. This is contrast to fluctuation fields caused by individual lattice defects in truss networks, which are significantly more local (Beex et al., 2011). If we consider the global error for in-plane bending, it can be observed that global error reduces for an increasing size of the fully resolved region, but the relative error remains at the same order of magnitude which is significant. For the 3D test case in which out-of-plane bending is considered, both errors are significantly large for the conforming triangulations with linear interpolation.

The two error measures of the non-conforming triangulations with linear interpolation of the kinematic variables show the same trends as those of

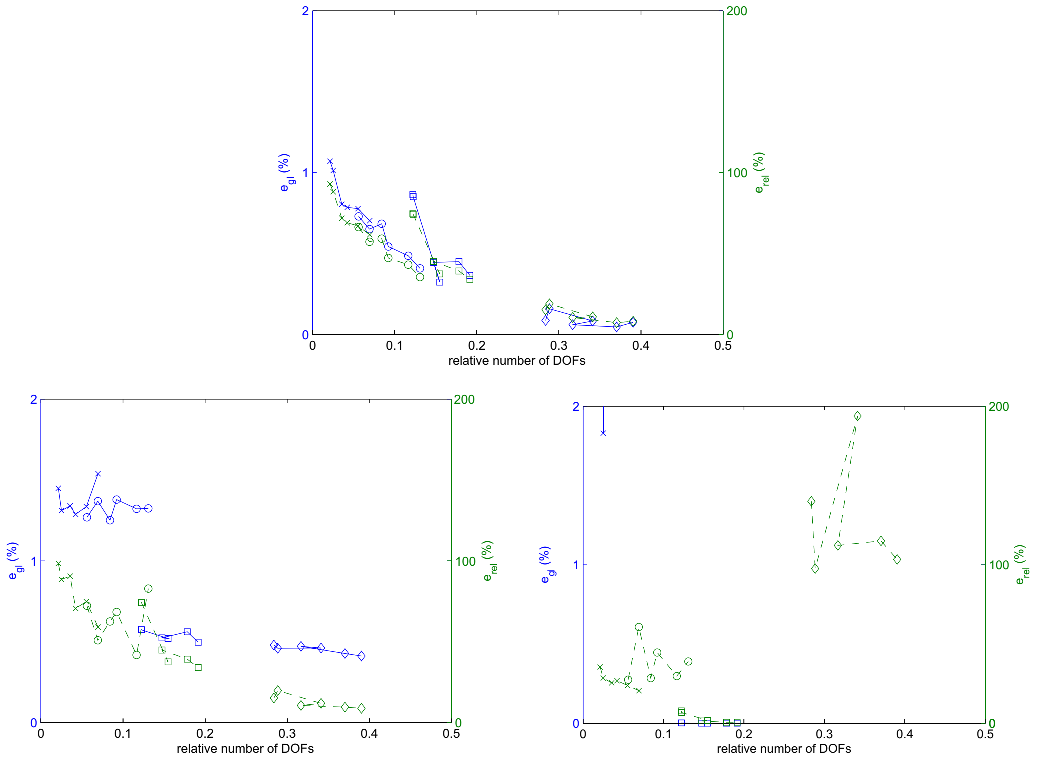

Figure 18: The global (e_{gl}, solid) and relative errors (e_{rel}, dashed) of the conforming triangulations with linear interpolation (○) and cubic interpolation of the displacements and quadratic interpolation of the rotations (◇) and of the non-conforming triangulations with linear interpolation (×) and cubic interpolation of the displacements and quadratic interpolation of the rotations (□) as a function of the relative number of DOFs. Top: uniform in-plane deformation, bottom-left: in-plane bending and bottom-right: out-of-plane bending.

the conforming triangulations with linear interpolation. The non-conforming triangulations use of course fewer DOFs and because of that the errors are larger.

The global and relative errors of the conforming triangulations with cubic interpolation of the displacements and quadratic interpolation of the displacements show a significant accuracy in Fig. 18 for the two 2D examples. For the 3D case however, the accuracy is so poor that it cannot be seen in the diagram.

The global and relative errors of the non-conforming triangulations with cubic interpolation of the displacements and quadratic interpolation of the displacements are substantially accurate for all the considered test cases (see Fig. 18). A condition for this is that the fully resolved region cannot be too small. An advantage of the fact that the non-conforming triangulations show sufficiently accurate results is that they use significantly fewer triangles than the non-conforming triangulations and hence, require significantly fewer sampling beams.

4.4. Full QC models: influence of interpolation and summation

Since only the non-conforming triangulations with cubic interpolation of the displacements and quadratic interpolation of the rotations give accurate results for all test cases, the influence of summation is investigated on that particular type of triangulation. As mentioned before, for higher order interpolations it is far from trivial how the potential energy depends on the interpolation. Therefore, sampling beams are selected near GQPs, as performed for 1D atomistic chains by Zhang and Gunzburger (2010) and Gunzburger and Zhang (2010). In this subsection, results are reported using 6, 7, 9 and 12, GQPs, but the accuracy is rather similar. For this reason, we suggest the use of 6 GQPs, because this hardly influences the accuracy and it selects as few sampling beams per triangle as possible (which is beneficial for the computational efficiency). A large discrepancy can however be observed for different triangulations (for 6, 7, 9 and 12 GQPs). As will be shown in this subsection, this stems from the selection of sampling beams that cross triangle edges. If a relatively large number of sampling beams are selected that cross triangle edges, the accuracy reduces.

For cubic finite elements it is sufficient to use 4 GQPs (Hughes, 1987), but the use of only 4 GQPs yields substantially inaccurate results. The reason for this is that one of the 4 GQPs is located exactly on the top of the central triangle nodes used for the cubic interpolation of the displacements, whereas the horizontal and vertical sampling beams selected near thes GQPs are never exactly located on top of them.

Therefore, the selection of sampling beams is investigated for the use of 6, 7, 9 and 12 GQPs. The location and weights of the GQPs can be found in Appendix B. The global and relative errors for these QC frameworks are presented in Fig. 19. The selection of sampling beams near 6, 7, 9 and 12 GQPs leads approximately to the same global and relative errors. However, significant changes can be observed for the same schemes for different triangulations. For instance, the selection of sampling beams near 6 GQPs using the non-conforming triangulation with a fully resolved region of 10 × 10 unit cells results in a significantly better accuracy than the non-conforming triangulation with a fully resolved region of 14 × 14 unit cells. This is remarkable, because it is generally observed in QC frameworks that an increase of the fully resolved region leads to an improved accuracy.

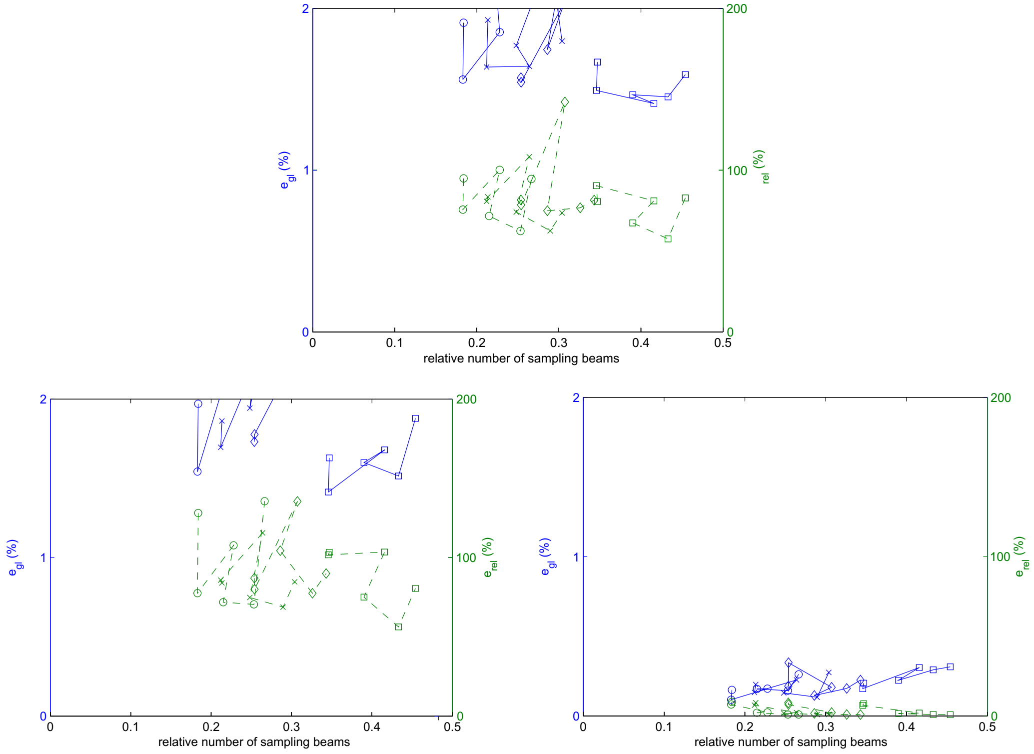

Figure 19: The global (e_{gl}, solid) and relative errors (e_{rel}, dashed) of the non-conforming triangulations with cubic interpolation of the displacements and quadratic interpolation of the rotations and sampling beams near 6 ($\circ$), 7 ($\times$), 9 ($\Box$) and 12 GQPs ($\diamond$).

The reason for this appears to be the fact that more small triangles are used in the non-conforming triangulation with a fully resolved region of 14 × 14 unit cells than in the non-conforming triangulation with a fully resolved region of 10 × 10 unit cells. For the non-conforming triangulation with a fully resolved region of 14 × 14 unit cells this leads to a (relatively as well as absolute) larger number of sampling beams that cross triangle edges than for the non-conforming triangulation with a fully resolved region of 10 × 10 unit cells. This is shown in Fig. 20.

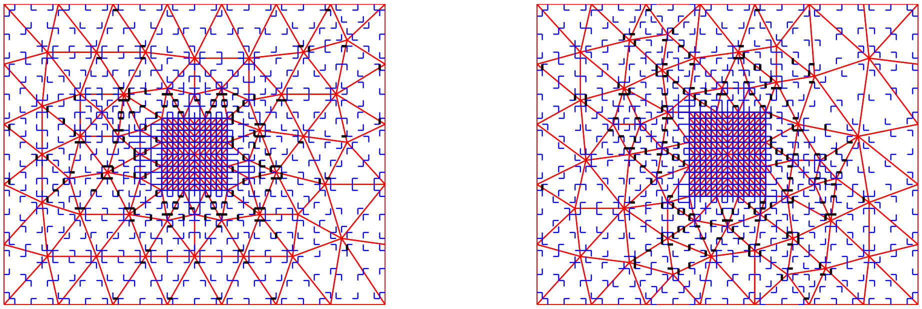

Figure 20: The sampling beams near 6 GQPs for the non-conforming triangulations with fully resolved regions of 10×10 (left) and 14×14 unit cells (right) from Fig. 14. Sampling beams that are located inside the same triangles are shown as thin blue lines and sampling beams that cross triangle edges are shown as thick black lines.

4.5. Full QC models: final framework

In this subsection, we propose the use of triangulations with cubic interpolation of the nodal displacements and quadratic interpolation of the nodal rotations in combination with the selection of sampling beams near 6 GQPs. Furthermore, to ensure that as few sampling beams as possible are selected that cross triangle edges, the interpolation triangles (not those in the fully resolved region obviously) must be relatively large. Although the relative error in the 2D test cases, which is governed by an extremely non-local fluctuation field in contrast to truss networks with a similar lattice defect, cannot be reduced as far as would be desired, this QC method gives the most accurate results for all three test cases.

To ensure that hardly any sampling beams are selected that cross triangle edges, non-conforming triangulations with relatively large triangles in the coarse domain are investigated. These non-conforming triangulations with fully resolved regions of 8×8, 10×10, 12×12 and 14×14 are shown in Fig. 21 together with the selection of the sampling beams. Clearly, significantly less sampling beams that cross triangle edges are selected. No non-conforming triangulations with fully resolved regions of 4×4 and 6×6 are investigated, because they could not be generated using the automatic triangulation procedure due to the large discrepancy between the small fully resolved regions and required size of the coarse triangles.

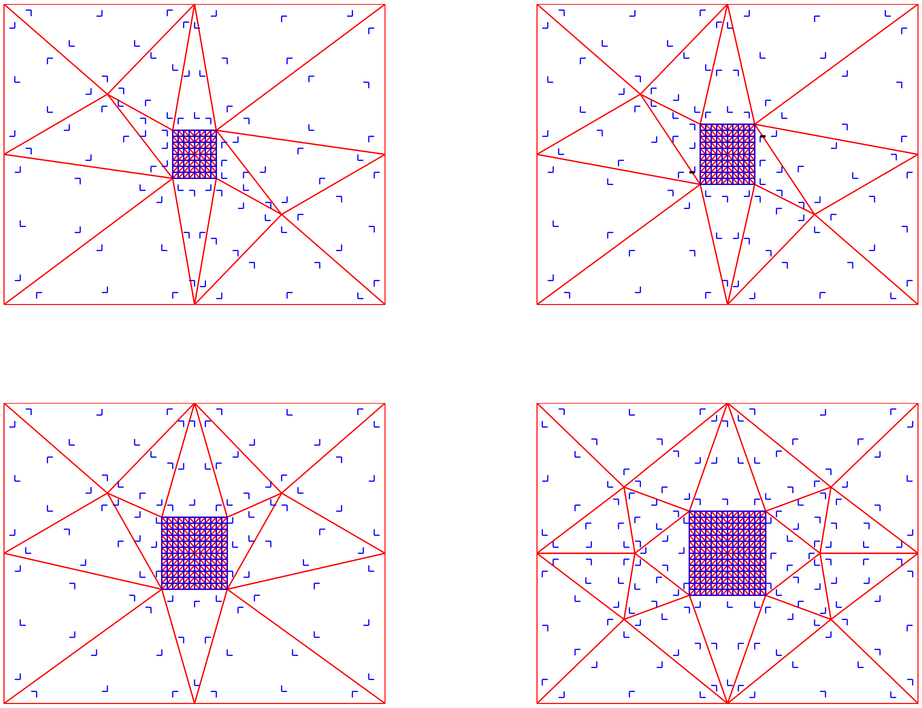

Figure 21: The sampling beams near 6 GQPs for the non-conforming triangulations with relatively large coarse triangles and fully resolved regions of 8 × 8 (top-left), 10 × 10 (top-right), 12 × 12 (bottom-left) and 14 × 14 unit cells (bottom-right). Sampling beams that are located inside the same triangles are shown as thin blue lines and sampling beams that cross triangle edges are shown as thick black lines.

Some indicative results for the non-conforming triangulation with a fully resolved region of 14 × 14 unit cells shown in Fig. 21 are presented in Fig. 22. The presented, absolute kinematic variables correspond well to those predicted by the direct lattice computations. The presented, relative kinematic variables for the 2D numerical examples correspond to a lesser extent with those predicted by the direct lattice computations. The reason is that the fluctuation induced by the single lattice defect is significantly non-local for the 2D examples. Since relatively large triangles are required in the coarse domain, this non-local fluctuation field given by the relative kinematic variables cannot be captured as accurately as the absolute kinematic variables.

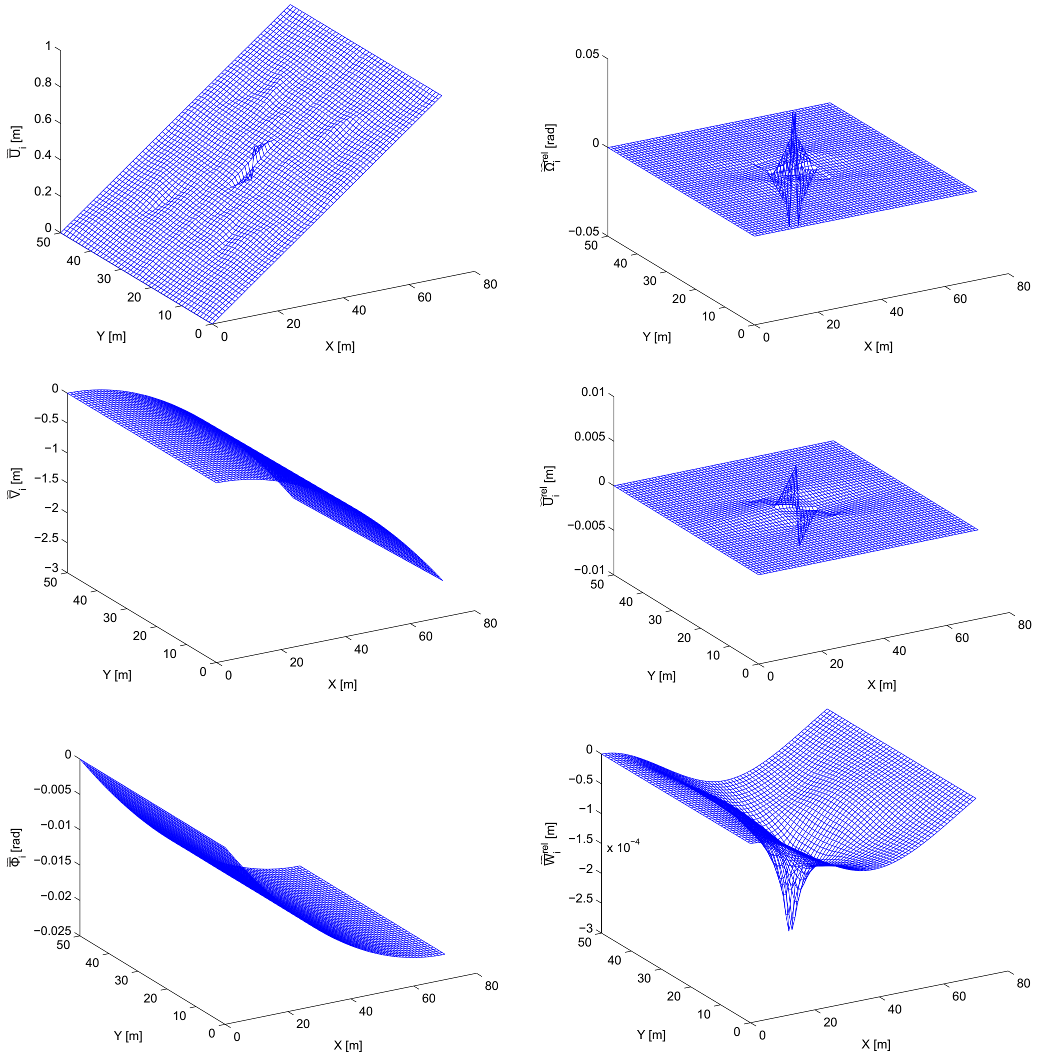

Figure 22: The horizontal displacements ($\tilde{\bar{U}}_i$, top-left) and the relative rotations around the Z-axis ($\tilde{\bar{\Omega}}_i^{rel}$, top-right) for uniform in-plane deformation, the vertical displacements ($\tilde{\bar{V}}_i$, center-left) and the relative horizontal displacements ($\tilde{\bar{U}}_i^{rel}$, center-right), and the rotations around the Y-axis ($\tilde{\bar{\Phi}}_i$, bottom-left) and the relative displacements in Z-direction ($\tilde{\bar{W}}_i^{rel}$, bottom-right) predicted by the QC framework using 6 GQPs for the non-conforming triangulation with a fully resolved region of 14×14 unit cells shown in Fig. 21.

The global and relative errors using the QC framework for non-conforming triangulations selecting sampling beams near 6 GQPs are presented in Fig. 23 for the three numerical examples. The diagrams show significantly small global errors for all three examples. They support the observation that the non-local fluctuation fields present in the relative kinematic variables can only be captured to a limited extent by the QC frameworks due to large triangles required in the coarse domain. Because the fluctuation field occurring in the 3D test case is significantly more local, it can be captured accurately.

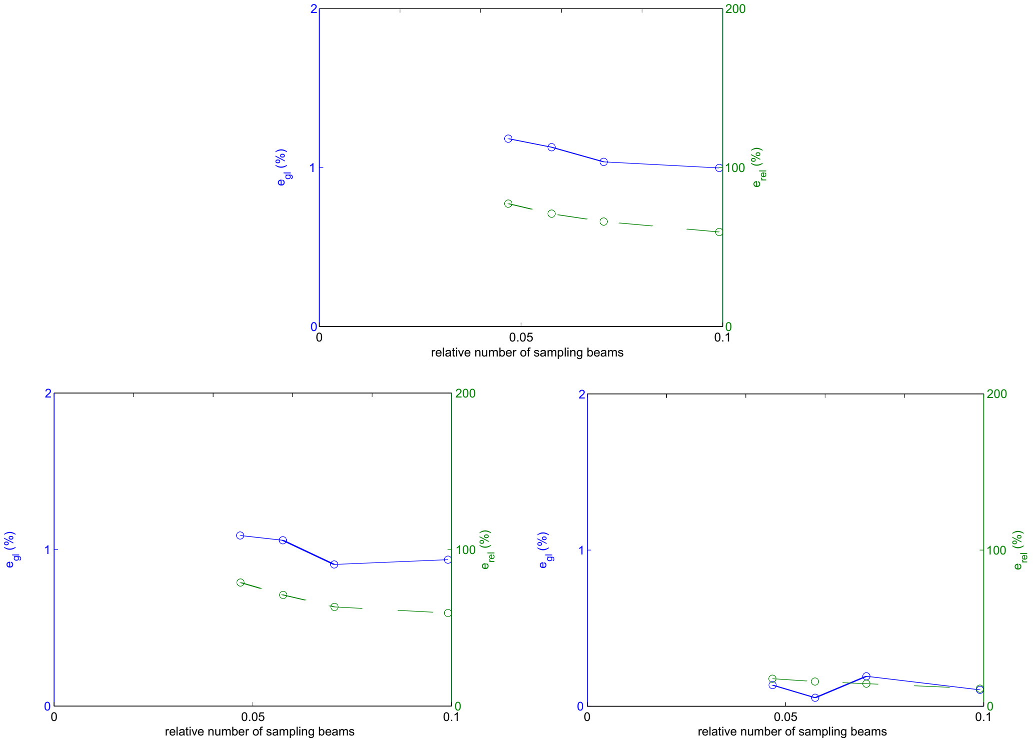

Figure 23: The global (e_{gl}, solid) and relative errors (e_{rel}, dashed) using the non-conforming triangulations shown in Fig. 21 with cubic interpolation of the displacements and quadratic interpolation of the rotations and sampling beams near 6 GQPs (○) for in-plane uniform deformation (top), in-plane bending (bottom-left) and out-of-plane bending (bottom-right).

Although the final QC framework for planar beam lattices is not able to capture the fluctuation fields of the relative kinematic variables particularly accurately due to the required large triangles in the coarse domains and the extreme non-locality of the fluctuations, the method requires a significantly smaller number of sampling beams - which are a good estimate of the saved computational time (Beex et al., 2014a). Since the modelling domain in the numerical examples is substantially small, the computational gain will be even larger for larger domains. Furthermore, the QC framework is accurate for 2D as well as 3D examples.

5. Conclusion

The QC method is a multiscale approach to reduce the computational costs of discrete lattice computations. The method allows the incorporation of local lattice phenomena (e.g. a single lattice defect) in macroscale simulations. The use of QC frameworks to reduce the computational costs of planar lattices consisting of Euler-Bernoulli beams is investigated in this study. QC frameworks have the advantage that they do not require the construction and calibration of a continuum description in coarse domains. Also no coupling procedures or handshaking methods need to be formulated to couple coarse domains to fully resolved domains.

In contrast to the kinematic variables of spring lattices such as atomistic lattices, the kinematic variables in beam lattices include nodal rotations next to nodal displacements. In the presented frameworks the rotations are interpolated as well. Linear interpolation of the nodal displacements as well as the nodal rotations results in large errors, because linear interpolation is not able to capture out-of-plane deformation of Euler-Bernoulli beam lattices accurately. Furthermore, the fluctuation fields caused by the single lattice defect are significantly non-local - in contrast to the fluctuation fields caused by a single lattice defect in spring lattices (Beex et al., 2011) - which cannot be accurately captured by linear interpolation.

In order to capture the out-of-plane deformation in an accurate manner, cubic interpolation of the nodal displacements and quadratic interpolation of the nodal rotations is investigated. For conforming triangulations - as generally used in QC methods - this leads to ill-posed systems because more kinematic variables are present in small interpolation triangles than governed by the underlying beam lattice. The GMRES algorithm (Saad and Schultz, 1986) can deal with ill-posed systems, but the results are insufficiently accurate. If non-conforming triangulations are used where in the coarse domains the nodal displacements and nodal rotations are interpolated cubically and quadratically, respectively, and if both types of kinematic variables are interpolated linearly in the fully resolved domains, the systems are well posed and significantly accurate results can be obtained for in-plane and out-of-plane deformations.

Summation rules that select sampling beams near 4, 6, 7, 9 and 12 Gaussian quadrature points (GQPs) are investigated for the non-conforming triangulations using cubic interpolation of the nodal displacements and quadratic interpolation of the nodal rotations. The results are similarly accurate for the use of 6, 7, 9 or 12 GQPs. Hence, to increase the computational efficiency as much as possible, the use of 6 GQPs is suggested. A demand for significantly accurate results for the applied in-plane and out-of-plane test cases is that the triangles in the coarse domain are significantly large so that no sampling beams cross triangle edges.

With the final QC framework that uses non-conforming triangulations, interpolates the nodal displacements cubically and the nodal rotations quadratically and selects sampling beams near 6 GQPs per triangle, significantly accurate results are obtained for all three multiscale test cases. These are summarised in Fig. 24. The relative error, which measures the relative fluctuation field caused by a single lattice defect, is a extremely stringent error measure, and although it seems large for the in-plane test cases, it is acceptable and other multiscale approaches do not determine such a error measure, e.g. because they are based on homogenization and do not capture local defects (Zhang et al., 2010; Gonella and Ruzzene, 2008). The requirement of using fairly large triangles in the coarse domain also leads to substantial computational savings in terms of the number of sampling beams; the most important means to measure the computational gain. Since the used numerical examples only demand a small modelling domain, the expected computational gain is even larger for increasing domains.

Although not investigated in this contribution, it may be more beneficial for implementation purposes to interpolate the nodal rotations cubically, similarly to the nodal displacements. It is expected that this will hardly influence the accuracy, since the quadratic interpolation field is part of the cubic interpolation field. Also the efficiency is expected not be influenced by this, since it will not influence the number of sampling beams. After all, the use of 6 GQPs is already required to accurately sample the lattice for the cubic interpolation of the nodal displacements. To implement the framework however, it may be easier to use cubic interpolation of the nodal displacements and nodal rotations.

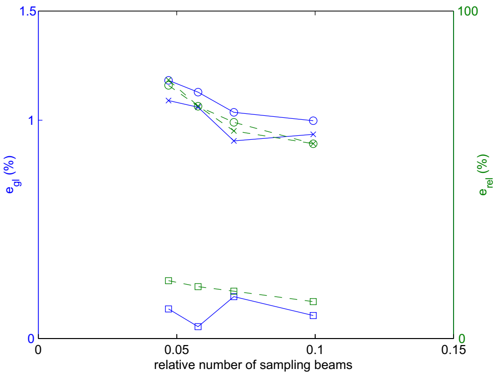

Figure 24: The global (e_{gl}, solid) and relative errors (e_{rel}, dashed) as a function of the relative number of sampling beams of the final QC framework for uniform in-plane deformation (○), in-plane bending (×) and out-of-plane bending (□) including an individual lattice defect.

Acknowledgements

Lars Beex, Pierre Kerfriden and Stephane Bordas would like to acknowledge partial financial support of the Framework Programme 7 Initial Training Network Funding under grant number 289361 "Integrating Numerical Simulation and Geometric Design Technology", of the EPSRC grant "Towards rationalised computational expense for simulating fracture over multiple scales (RationalMSFrac)" and of the Cardiff Institute for Mechanics and Advanced Materials.

A. Potential energy of an Euler-Bernoulli beam

In this appendix, the potential energy of lattice interaction i (E_i in Eq. (3)) is derived in terms of the (global) kinematic variables ($\mathbf{a} = [\mathbf{U}^T\ \mathbf{\Theta}^T]^T$). The beam lattice as shown in Fig. 1, and thus also the beam in Fig. 25, is located in the X-Y plane. The lattice beams have a rectangular cross-section. The beam in Fig. 25 is connected between lattice nodes i and j, which are locally defined as nodes 1 and 2. The axes of the global coordinate system are indicated by X, Y and Z, respectively. Global displacements are indicated by U, V and W in the X-direction, Y-direction and Z-direction, respectively. Global rotations indicated by Θ, Φ and Ω are defined as clockwise rotations around the X-axis, Y-axis and Z-axis, respectively. In the same fashion local beam axes, local beam displacements and local beam rotations are indicated by x, y, z, and u, v, w, and θ, ϕ and ω, respectively. The subscripts refer to the displacements and rotations at the local beam nodes. The beam is of length L in x-direction, thickness t in y-direction and height h in z-direction. The plane of the planar beam lattice corresponds the X-Y plane. An initial rotation of the beam is present, indicated by Ω_0. Note that Ω_0 is positive, since the rotations are defined as clockwise rotations around the associated axes.

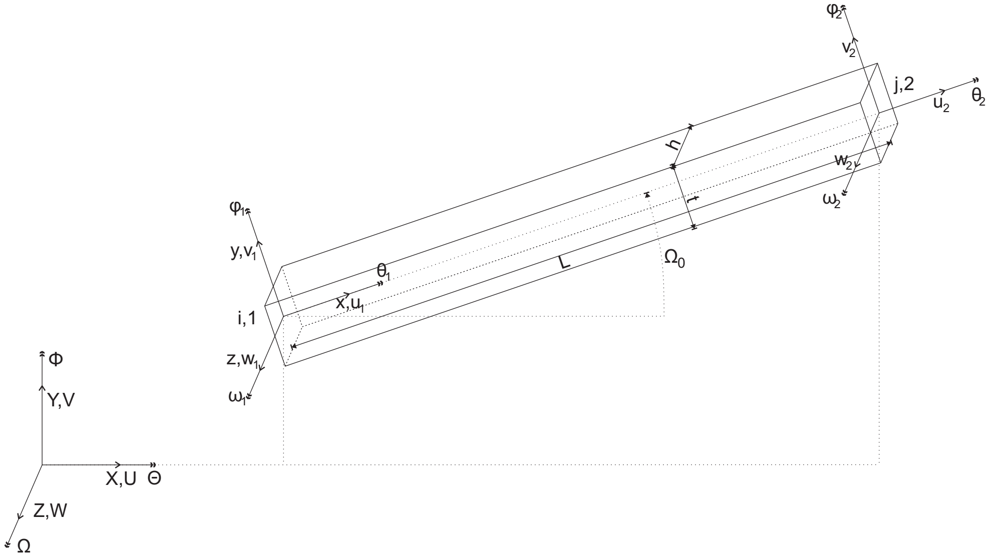

Figure 25: Schematic representation of a beam in the planar beam lattice.

The beams in the lattice consist of a linear elastic isotropic material and undergo small deformations. As assumed in traditional Euler-Bernoulli beam theory (Han et al., 1999), the deformation modes of the beams do not influence each other, although some studies do not use this assumption, see e.g. (Karihaloo et al., 2003). As a result of the independence of the deformation modes, they can be superimposed. This leads to the following expression of the potential energy of Euler-Bernoulli beam i, E_i:

$$E_i = \frac{Y}{2} \int_0^L \int_{-\frac{t}{2}}^{\frac{t}{2}} \int_{-\frac{h}{2}}^{\frac{h}{2}} \Big(\epsilon_{xx/ud} + \epsilon_{xx/bz} + \epsilon_{xx/by} \Big)^2 + \frac{\gamma_{xy}^2 + \gamma_{xz}^2}{2(1+\nu)} \, dzdydx, \quad (25)$$

where Y and ν are the Young's modulus and the Poisson's ratio, respectively. Furthermore, $\epsilon_{xx/ud}$, $\epsilon_{xx/bz}$ and $\epsilon_{xx/by}$ are the normal strains in x-direction due to uniform deformation in x-direction, bending around the z-axis and bending around the y-axis, respectively. The shear strains occurring due to torsion around the x-axis are represented by γ_{xy} and γ_{xz}, respectively. If we now express the strains in terms of the kinematic variables that are linearly interpolated over the x-axis (i.e. the longitudinal displacements and torsional rotations), the following formulation is obtained:

$$\begin{aligned} E_i = \frac{Y}{2}\int_0^L \int_{-\frac{t}{2}}^{\frac{t}{2}} \int_{-\frac{h}{2}}^{\frac{h}{2}} \left(\frac{u_2 - u_1}{L} - y\frac{\partial^2 v}{\partial x^2} - z\frac{\partial^2 w}{\partial x^2}\right)^2 + \\ \left(\frac{\theta_2 - \theta_1}{L}\right)^2 \frac{y^2 + z^2}{2(1+\nu)}\, dzdydx. \end{aligned} \tag{26}$$

Hermite interpolation is used to interpolate the beam deflections and bending angles in beam theory. It interpolates the beam deflections cubically and bending angles quadratically and effectively expresses the bending deflections and rotation angles over the x-axis of a beam in terms of the nodal deflections and nodal bending angles $(v_1, v_2, w_1, w_2, \phi_1, \phi_2, \omega_1, \omega_2)$. This type of interpolation uses the assumption made in Euler-Bernoulli beam theory that the bending angles are the derivatives of the beam deflections. The deflections, v and w, are cubic functions in the longitudinal (x-)direction of the beam and thus can be expressed as follows:

$$\begin{aligned} v(x) &= c_{v1}x^3 + c_{v2}x^2 + c_{v3}x + c_{v4} \\ w(x) &= c_{w1}x^3 + c_{w2}x^2 + c_{w3}x + c_{w4}, \end{aligned} \tag{27}$$

The different constants ($c_{v1}, ..., c_{v4}$ and $c_{w1}, ..., c_{w4}$), can be expressed in terms of the local nodal deflections and rotations (v_1, v_2, ω_1, ω_2, w_1, w_1, ϕ_1 and ϕ_2) by solving the following equations:

$$\begin{aligned} v(x=0) = v_1 \quad v(x=L) = v_2 \quad \left.\frac{\partial v}{\partial x}\right|_{x=0} = \omega_1 \quad \left.\frac{\partial v}{\partial x}\right|_{x=L} = \omega_2 \\ w(x=0) = w_1 \quad w(x=L) = w_2 \quad \left.\frac{\partial w}{\partial x}\right|_{x=0} = -\phi_1 \quad \left.\frac{\partial w}{\partial x}\right|_{x=L} = -\phi_2. \end{aligned} \tag{28}$$

Substitution of $\frac{\partial^2 v}{\partial x^2}$ and $\frac{\partial^2 w}{\partial x^2}$ in Eq. (26) expresses E_i as a function of the local kinematic variables. The orientation of the beam in terms of the global coordinate system must be used to express E_i as a function of the global kinematic variables. This leads to the following formulation for the kinematic variables of node i (local node 1):

$$\begin{bmatrix} u_1 \\ v_1 \\ w_1 \\ \theta_1 \\ \phi_1 \\ \omega_1 \end{bmatrix} = \begin{bmatrix} \cos\Omega_0 & \sin\Omega_0 & 0 & 0 & 0 & 0 \\ -\sin\Omega_0 & \cos\Omega_0 & 0 & 0 & 0 & 0 \\ 0 & 0 & 1 & 0 & 0 & 0 \\ 0 & 0 & 0 & \cos\Omega_0 & \sin\Omega_0 & 0 \\ 0 & 0 & 0 & -\sin\Omega_0 & \cos\Omega_0 & 0 \\ 0 & 0 & 0 & 0 & 0 & 1 \end{bmatrix} \begin{bmatrix} U_i \\ V_i \\ W_i \\ \Theta_i \\ \Phi_i \\ \Omega_i \end{bmatrix}. \tag{29}$$

B. Locations and weights of Gaussian quadrature points

The locations and weights of Gaussian quadrature points as used in FE technologies are shown in Table 2, which is adopted from Hughes (1987). Although the four GQP rule is not used, it is included in the table to present that one of the GQPs is located in the center of a triangle as reported in section 3.2.1. The locations of the GQPs in Table 2 are presented in terms of the barycentric coordinates, λ_1, λ_2 and λ_3, which are indicated in Fig. 26.

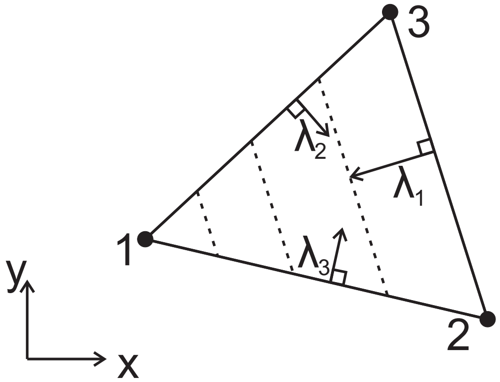

Figure 26: Schematic representation of the barycentric coordinates, λ_1, λ_2 and λ_3, in a triangle that is spanned by nodes 1, 2 and 3. Some lines for a constant λ_1 are shown by dashed lines. The Z-direction is not included, since all triangles are obviously located in the X-Y plane, similar to the beam lattice.

Table 2: Locations and weights of GQPs of the four-point rule, six-point rule, seven-point rule, nine-point rule and twelve-point rule for triangular finite elements as used in this study. This table is adopted from Hughes (1987).

Rule	w_{GQP}	λ_1	λ_2	λ_3
4	-0.56250 00000	0.33333 33333	0.33333 33333	0.33333 33333
	0.52083 33333	0.60000 00000	0.20000 00000	0.20000 00000
	0.52083 33333	0.20000 00000	0.60000 00000	0.20000 00000
	0.52083 33333	0.20000 00000	0.20000 00000	0.60000 00000
6	0.10995 17437	0.81684 75730	0.09157 62135	0.09157 62135
	0.10995 17437	0.09157 62135	0.81684 75730	0.09157 62135
	0.10995 17437	0.09157 62135	0.09157 62135	0.81684 75730
	0.22338 15897	0.10810 30182	0.44594 84909	0.44594 84909
	0.22338 15897	0.44594 84909	0.10810 30182	0.44594 84909
	0.22338 15897	0.44594 84909	0.44594 84909	0.10810 30182
7	0.22500 00000	0.33333 33333	0.33333 33333	0.33333 33333
	0.12593 91805	0.79742 69854	0.10128 65073	0.10128 65073
	0.12593 91805	0.10128 65073	0.79742 69854	0.10128 65073
	0.12593 91805	0.10128 65073	0.10128 65073	0.79742 69854
	0.13239 41527	0.05971 58718	0.47014 20641	0.47014 20641
	0.13239 41527	0.47014 20641	0.05971 58718	0.47014 20641
	0.13239 41527	0.47014 20641	0.47014 20641	0.05971 58718
9	0.20595 05048	0.12494 95032	0.43752 52484	0.43752 52484
	0.20595 05048	0.43752 52484	0.12494 95032	0.43752 52484
	0.20595 05048	0.43752 52484	0.43752 52484	0.12494 95032
	0.06369 14143	0.79711 26519	0.16540 99274	0.03747 74208
	0.06369 14143	0.79711 26519	0.03747 74208	0.16540 99274
	0.06369 14143	0.16540 99274	0.79711 26519	0.03747 74208
	0.06369 14143	0.03747 74208	0.79711 26519	0.16540 99274
	0.06369 14143	0.16540 99274	0.03747 74208	0.79711 26519
	0.06369 14143	0.03747 74208	0.16540 99274	0.79711 26519
12	0.05084 49064	0.87382 19710	0.06308 90145	0.06308 90145
	0.05084 49064	0.06308 90145	0.87382 19710	0.06308 90145
	0.05084 49064	0.06308 90145	0.06308 90145	0.87382 19710
	0.11678 62757	0.50142 65097	0.24928 67452	0.24928 67452
	0.11678 62757	0.24928 67452	0.50142 65097	0.24928 67452
	0.11678 62757	0.24928 67452	0.24928 67452	0.50142 65097
	0.08285 10756	0.63650 24991	0.31035 24510	0.05314 50498
	0.08285 10756	0.63650 24991	0.05314 50498	0.31035 24510
	0.08285 10756	0.31035 24510	0.63650 24991	0.05314 50498
	0.08285 10756	0.05314 50498	0.63650 24991	0.31035 24510
	0.08285 10756	0.31035 24510	0.05314 50498	0.63650 24991
	0.08285 10756	0.05314 50498	0.31035 24510	0.63650 24991

References

Argento, G., Simonet, M., Oomens, C.W.J., Baaijens, F.P.T., 2012, Multiscale mechanical characterization of scaffolds for heart valve tissue engineering, Journal of Biomechanics, Vol. 45, 2893-2898.

Beex, L.A.A., Peerlings, R.H.J., Geers, M.G.D., 2011, A quasicontinuum methodology for multiscale analyses of discrete microstructures, International Journal for Numerical Methods in Engineering, Vol. 46, 4192-4207.

Beex, L.A.A., Verberne, C.W, Peerlings, R.H.J., 2013a, Experimental identification of a lattice model for woven fabrics: application to electronic textile, Composites Part A, Vol. 48, 82-92.

Beex, L.A.A., Peerlings, R.H.J., Geers, M.G.D., Central summation in the quasicontinuum method, Journal of the Mechanics and Physics of Solids, Accepted.

Beex, L.A.A., Peerlings, R.H.J., Geers, M.G.D., 2014a, A multiscale quasicontinuum method for dissipative lattice models and discrete networks, Journal of the Mechanics and Physics of Solids, Vol. 64, 154-169.

Beex, L.A.A., Peerlings, R.H.J., Geers, M.G.D., 2014b, A multiscale quasicontinuum framework for lattice models with bond failure and fiber sliding, Computer Methods in Applied Mechanics and Engineering, Vol. 269, 108-122.

Ben Boubaker, B., Haussy, B., Ganghoffer, J.F., 2007, Discrete models of woven structures. Macroscopic approach, Composites: Part B, Vol. 38, 498-505.

Berinskii, I., Borodich, F.M., 2013, Elastic in-plane properties of 2D linearized models of graphene, Mechanics of Materials, Vol. 62, 60-68.

Bronkhorst, C.A., 2003, Modelling paper as a two-dimensional elastic-plastic stochastic network, International Journal of Solids and Structures, Vol. 40, 5441-5454.

Brown, P.N., Walker, H.F., 1997, GMRES on (nearly) singular systems, SIAM Journal on Matrix Analysis and Applications, Vol. 18, 37-51.

Chandran, P.L., Barocas, V.H., 2006, Affine versuse non-affine fibril kinematics in collagen networks: theoretical studies of network behavior, Journal of Biomechanical Engineering, Vol. 128, 259-270.

Curtin, W.A., Miller, R.E., 2003, Atomistics/continuum coupling in computational materials science, Modelling and Simulation in Materials Science and Engineering, Vol. 11, 33-68.

Desphande, V.S., Fleck, N.A., Ashby, M.F., 2001, Effective properties of the octet-truss lattice material, Journal of the Mechanics and Physics of Solds, Vol. 49, 1747-1769.

Dobson, M., Elliott, R.S., Luskin, M., Tadmor, E.B., 2012, A multilattice quasicontinuum for phase transforming materials: cascading Cauchy-Born kinematics, Journal of Computer-Aided Materials Design, Vol. 14, 219-237.

Eidel, B., Stukowski, A., 2009, A variational form of the quasicontinuum method based on energy sampling in clusters, Journal of the Mechanics and Physics of Solids, Vol. 57, 87-108.

Fish, J., Nuggehally, M.A., Shephard, M.S., Picu, C.R., Badia, S., Parks, M.L., Gunzburger, M., 2007, Concurrent AtC coupling based on a blend of the continuum stress and the atomistic force, Computer Methods in Applied Mechanics and Engineering, Vol. 196, 4548-4560.

Fleck, N.A., Qiu, X., 2007, The damage tolerance of elastic-brittle two-dimensional isotropic lattices, Journal of the Mechanics and Physics of Solids, Vol. 55, 562-588.

Gunzburger, M., Zhang, Y., 2010, A quadrature-type approximation to the quasi-continuum method, Multiscale Modeling and Simulation, Vol. 8, 571-590.

Han, S.M., Benaroya, H., Wei, T., 1999, Dynamics of transversely vibrating beams using four engineering theories, Journal of Sound and Vibration, Vol. 225, 935-988.

Heyden, S., 2000, Network modelling for the evaluation of mechanical properties of cellulose fibre fluff, Doctoral thesis, Lund University, Lund, Sweden.

Hughes, T.J.R., 1987, The finite element method: linear static and dynamic finite element analysis, Prentice-Hall Inc., Englewood Cliffs, New Jersey, USA.

Gonella, S., Ruzzene, M., 2008, Homogenization and equivalent in-plane properties of two-dimensional periodic lattices, International Journal of Solids and Structures, Vol. 45, 2897-2915.

Ince, R., Arslan, A., Karihaloo, B.L., 2002, An improved lattice model for concrete fracture, ASCE Journal of Engineering Mechanics, Vol. 128, 57-66.

Intrigila, B., Melatti, I., Tofani, A., Macchiarelli, G., 2007, Computational models of myocardial endomysial collagen arrangement, Computer Methods and Programs in Biomedicine, Vol. 86, 243-244.

Karihaloo, B.L., Shao, P.F., Xiao, Q.Z., 2003, Lattice modelling of the failure of particulate composites, Engineering Fracture Mechanics, Vol. 70, 2385-2406.

Kerfriden, P., Gosseleet, P., Adhikari, S., Bordas, S.P.A., 2011, Bridging proper orthogonal decomposition methods and augmented NewtonKrylov algorithms: An adaptive model order reduction for highly nonlinear mechanical problems, Computer Methods in Applied Mechanics and Engineering, Vol. 200, 850-866.

Kerfriden, P., Passieux, J.C., Bordas, S.P.A., 2012, Local/global model order reduction strategy for the simulation of quasi-brittle fracture, International Journal for Numerical Methods in Engineering, Vol. 89, 154-179.

Kerfriden, P., Goury, O., Rabczuk, T., Bordas, S.P.A., 2013a, A partitioned model order reduction approach to rationalise computational expenses in nonlinear fracture mechanics, Computer Methods in Applied Mechanics and Engineering, Vol. 256, 169-188.

Kerfriden, P., Schmidt, K.M., Rabczuk, T., Bordas, S.P.A., 2013b, Statistical extraction of process zones and representative subspaces in fracture of random composite, International Journal for Multiscale Computational Engineering, Vol. 11, 253-287.

Klein, P.A., Zimmerman, J.A., 2006, Coupled atomistic-continuum simulations using arbitrary overlapping domains, Journal of Computational Physics, Vol. 213, 86-116.

Knap, J., Ortiz, M., 2001, An analysis of the quasicontinuum method, Journal of the Mechanics and Physics of Solids, Vol. 49, 1899-1923.

Kulachenko, A., Uesaka, T., 2012, Direct simulation of fiber network deformation and failure, Mechanics of Materials, Vol. 51, 1-14.

Lilliu, G., Van Mier, J.G.M., 2007, On the relative use of micro-mechanical lattice analysis of 3-phase particle composites, Engineering Fracture Mechanics, Vol. 74, 1174-1189.

Lomov, S.V., Ivanov, D.S., Verpoest, S., Zako, M., Kurashiki, T., Nakai, H., Hirosawa, S., 2007, Meso-FE modelling of textile composites: Road map, data flow and algorithms, Composite Science and Technology, Vol. 67, 1870-1891.

Miller, R., Ortiz, M., Phillips, R., Shenoy, V., Tadmor, E.B., 1998, Quasicontinuum models of fracture and plasticity, Engineering Fracture Mechanics, Vol. 61, 427-444.

Miller, R.E., Tadmor, E.B., 2002, The quasicontinuum method: overview, applications and current directions, Journal of Computer-Aided Materials Design, Vol. 9, 203-239.

Ostoja-Starzewski, M., 2002, Lattice models in micromechanics, Applied Mechanics Reviews, Vol. 55, 35-60.

Peerlings, R.H.J., Javani, H.R., Mediavilla, J., Geers, M.G.D., 2008, Modelling of damage initiation and propagation in metal forming, International Journal of Material Forming, Vol. 1, 1123-1126.

Persson, J., Isaksson, P., 2013, A particle-based method for mechanical analyses of planar fiber-based materials, International Journal for Numerical Methods in Engineering, Vol. 93, 1216-1234.

Ridruejo, A., Gonzáez, C., LLorca, J., 2010, Damage micromechanisms and notchsensitivity of glass-fiber non-woven felts: an experimental and numerical study, Journal of the Mechanics and Physics of Solids, Vol. 58, 1628-1645.

Ridruejo, A., Gonzáez, C., LLorca, J., 2012, Damage localization and failure locus under biaxial loading in glass-fiber nonwoven felts, Journal of Multiscale Computational Engineering, Vol. 10, 425-440.

Ryvkin, M., Slepyan, L., 2010, Crack in a 2D beam lattice: analytical solutions for two bending modes, Journal of the Mechanics and Physics of Solids, Vol. 58, 902-917.

Saad, Y., Schultz, M.H., 1986, GMRES: A generalized minimal residual algorithm for solving nonsymmetric linear systems, SIAM Journal on Scientific and Statistical Computing, Vol. 7, 856-869.

Shenoy, V.B., Miller, R., Tadmor, E.B., Rodney, D., Phillips, R., Ortiz, M., 1999, An adaptive finite element approach to atomistic scale mechanics-the quasicontinuum method, Journal of the Mechanics and Physics of Solids, Vol. 47, 611-642.

Shimokawa, T., Mortensen, J.J., Schiøtz, J., Jacobsen, K.W., 2004, Matching conditions in the quasicontinuum method: Removal of the error introduced at the interface between the coarse-grained and fully atomistic region, Physical Review B, Vol. 69, 214104.

Stylianopoulos, T., Barocas, V.H., 2007, Volume-averaging theory for the study of mechanics of collagen-networks, Computer Methods in Applied Mechanics and Engineering, Vol. 196, 2981-2990.

Tadmor, E.B., Philips, R., Ortiz, M., 1996, Mixed atomistics and continuum models of deformation in solids, Langmuir, Vol. 12, 4529-4534.

Tadmor, E.B., Ortiz, M., Philips, R., 1996, Quasicontinuum analysis of defects in solids, Philosophical Magazine A, Vol. 73, 1529-1563.

Wang, C.C., Lan, L., Liu, Y.P., Tan, H.F., He, X.D., 2013, Vibration characteristics of wrinkled single-layered graphene sheets, International Journal of Solids and Structures, Vol. 50, 1812-1823.

Wilbrink, D.V., Beex, L.A.A., Peerlings, R.H.J., 2013, A discrete network model for bond failure and frictional sliding in fibrous materials, International Journal of Solids and Structures, Vol. 50, 1354-1363.

Xiao, B.K., Belytschko, T., 2004, A bridging domain method for coupling continua with molecular dynamics, Computer Methods in Applied Mechanics and Engineering, Vol. 193, 1645-1669.

Yang, Q., Biyikli, E., To, A., 2013, Multiresolution molecular mechanics: statics, Computer Methods in Applied Mechanics and Engineering, Vol. 258, 26-38.

Zhang, Y., Gunzburger, M., 2010, Quadrature-rule type approximations to the quasicontinuum method for long-range interatomic interactions, Computer Methods in Applied Mechanics and Engineering, Vol. 199, 648-659.

Zhang, H.W., Wu, J.K., Fu, Z.D. 2010, Extended multiscale finite element method for mechanical analysis of periodic lattice truss materials, Journal for Multiscale Computational Engineering, Vol. 8, 597-613.